

AD-A274 454  
[REDACTED]

(2)

PL-TR-92-2173

## ADVANCES IN INFRARED INSTRUMENTATION

Wallace K. Wong  
James J. Guregian  
Holger M. Luther

SSG Inc  
150 Bear Hill Road  
Waltham, MA 02154

19 June 1992

DTIC  
ELECTE  
NOV 02 1992  
S P D

Final Report  
24 September 1985 - 31 March 1992

APPROVED FOR PUBLIC RELEASE; DISTRIBUTION UNLIMITED



PHILLIPS LABORATORY  
Directorate of Geophysics  
AIR FORCE SYSTEMS COMMAND  
HANSCOM AIR FORCE BASE, MA 01731-5000

Best Available Copy

93-26299

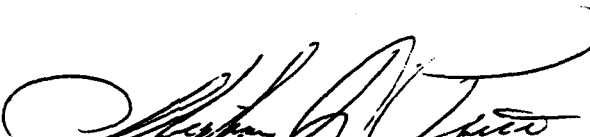
93-10 29031

This technical report has been reviewed and is approved for publication



---

FRANCIS X. ROBERT  
Contract Manager



---

STEPHAN D. PRICE  
Branch Chief



---

ROGER VAN TASSEL  
Division Director

This report has been reviewed by the ESC Public Affairs Office (PA) and is releasable to the National Technical Information Service (NTIS).

Qualified requestors may obtain additional copies from the Defense Technical Information Center. All others should apply to the National Technical Information Service.

If your address has changed, or if you wish to be removed from the mailing list, or if the addressee is no longer employed by your organization, please notify PL/TSI, Hanscom AFB, MA 01731-3010. This will assist us in maintaining a current mailing list.

Do not return copies of this report unless contractual obligations or notices on a specific document requires that it be returned.

# REPORT DOCUMENTATION PAGE

Form Approved  
OMB No. 0704-0188

Public reporting burden for this collection of information is estimated to average 1 hour per response, including the time for reviewing instructions, searching existing data sources, gathering and maintaining the data needed, and completing and reviewing the collection of information. Send comments regarding this burden estimate or any other aspect of this collection of information, including suggestions for reducing this burden, to Washington Headquarters Services, Directorate for Information Operations and Reports, 1215 Jefferson Davis Highway, Suite 1200, Arlington, VA 22202-4302, and to the Office of Management and Budget, Paperwork Reduction Project 0704-0188, Washington, DC 20583.

1. AGENCY USE ONLY (Leave Blank)	2. REPORT DATE	3. REPORT TYPE AND DATES COVERED	
	19 June 1992	Final Report - 850924 - 920331	
4. TITLE AND SUBTITLE			5. FUNDING NUMBERS
Advances in Infrared Instrumentation			PE 62101F PR 3054 TA 01 WU AC Contract F19628-85-C-0103
6. AUTHORS			
Wallace K. Wong James J. Guregian Dr. Holger Luther			
7. PERFORMING ORGANIZATION NAME(S) AND ADDRESS(ES)			8. PERFORMING ORGANIZATION REPORT NUMBER
SSG, Inc. 150 Bear Hill Road Waltham, MA 02154			
9. SPONSORING/MONITORING AGENCY NAME(S) AND ADDRESS(ES)			10. SPONSORING/MONITORING AGENCY REPORT NUMBER
Phillips Laboratory Hanscom Air Force Base Massachusetts 01731-5000  Contract Manager: Frank Robert / GPOB			PL-TR-92-2173
11. SUPPLEMENTARY NOTES			
12a. DISTRIBUTION/AVAILABILITY STATEMENT			12b. DISTRIBUTION CODE
Approved for public release; distribution unlimited.			
13. ABSTRACT (Maximum 200 words)			
<p>The goal of this project is to develop an IR spectrometer concept for spectral measurement of randomly occurring optical events for differentiation of man-made versus naturally occurring phenomenon such as lightning. Pulsewidth as short as 10 microseconds makes standard Michelson interferometer unsuitable. SSG investigated optical concepts with no moving parts by detection of a spatially extended optical fringe pattern with a linear detector array. Visible breadboard interferometer of "Tilted Michelson" and "Common Path Triangle" configurations were assembled and demonstrated successfully. We learned that although the randomly occurring test sources were detected, the SNR sensitivity was lower than expected - comparable to a single slit spectrometer using the same FPA. For increase of SNR, a novel photodiode array spectrometer concept using many entrance slots and encode them with a pattern in accordance with a Hadamard derived coding scheme was invented by VanTassel and Wong (U.S. Patent No. 5050989). A visible breadboard Hadamard Transform Spectrometer was also built to validate the sensitivity advantage over the single slit spectrometer.</p>			
14. SUBJECT TERMS			15. NUMBER OF PAGES
Fast Acquisition of Spectral Transients Hadamard Transform Spectrometer Contamination Degradation			84
16. PRICE CODE			
17. SECURITY CLASSIFICATION OF REPORT	18. SECURITY CLASSIFICATION OF THIS PAGE	19. SECURITY CLASSIFICATION OF ABSTRACT	20. LIMITATION OF ABSTRACT
Unclassified	Unclassified	Unclassified	SAR

## CONTENTS

<b>Program Scope</b>	<b>v</b>
<b>Part 1: Fast Acquisition of Spectral Transients</b>	<b>1</b>
<b>Signal-to-Noise Characteristics of Photodiode Array Fourier Transform Spectrometers</b>	<b>3</b>
<b>Hadamard-Coded, Stationary-Entrance-Mask, Photodiode-Array Spectrometer</b>	<b>5</b>
<b>Measured Performance of a Hadamard-Coded Photodiode-Array Spectrometer</b>	<b>13</b>
<b>Evaluation of a Hadamard-Coded Photodiode-Array Spectrometer Under Low Illumination</b>	<b>16</b>
<b>Part 2: Contamination Degradation Program</b>	<b>47</b>
<b>Part 3: Supersensitive IR Spectrometer for Spatial Measurements</b>	<b>58</b>

DTIC QUALITY ASSURANCE 5

Accession For	
NTIS GRA&I	<input checked="" type="checkbox"/>
DTIC TAB	<input type="checkbox"/>
Unannounced	<input type="checkbox"/>
Justification	
By _____	
Distribution/ _____	
Availability Codes	
Dist	Avail and/or Special
A-1	

## PROGRAM SCOPE

Three separate R&D efforts were conducted in this program. Advances resulting from this project are applicable to geographical research at the Phillips Laboratory.

### Topic 1: "Fast Acquisition of Spectral Transients"

Principal Investigator: Mr. Wallace K. Wong

The objective was the development of an interferometric spectrometer concept for detection of very-short-duration optical phenomena. The transient events of interest, as short as lightning stroke, say, can not be detected by the standard Michelson interferometers. The initial spectrometer concept is based on a no-moving part, "Tilted Michelson" or "Common-Path Triangle" configuration. A laboratory breadboard was demonstrated. An analysis of its advantage and shortcomings was published in a technical paper.

This research led to the development of another spectrometer concept for spectral transient detection. The new concept uses a Hadamard-coded multiple-slotted entrance aperture with a photodiode-array dispersive spectrometer. Three additional technical papers were published under this topic and a breadboard instrument was demonstrated.

### Topic 2: "Contamination Degradation Program"

Principal Investigator: Mr. James J. Guregian

The problem is the in situ characterization of contamination effects on clean, super-polished mirrors under vacuum conditions similar to space environments. The techniques and experimental results have led to a better understanding and data base on the Bi-directional Reflection Distribution Function (BRDF) of flight qualified mirrors. A long-duration mirror-exposure experiment was conceptualized, designed and assembled. Experimental data spanning over six (6) months were collected and analyzed.

### Topic 3. "Supersensitive IR Spectrometer for Spatial Measurements"

Principal Investigator: Dr. Holger M. Luther

This is a concept design and breadboard issue resolution effort to champion an advanced spectrometer approach. The study addresses the potential benefit of a cryogenic Fabry-Perot interferometer in front of a Rockwell Solid State Photomultiplier (SSPM) for a super-narrow bandpass detector. The critical components were identified and detail designs were proposed. The continuation of this effort was terminated when the STRAW mission was terminated (due to funding cuts).

The rest of this report is organized into three separate parts that cover the three topics above.

**Part 1.**

**Topic 1. Fast Acquisition of Spectral Transients**

**Principal Investigator: Mr. Wallace K. Wong**

The program goal is to develop the spectrometer concepts for "Fast Acquisition of Spectral Transients" a.k.a. "FAST". This involves the design and development of a no moving parts instrument for detection of very short duration optical phenomenon. Several optical designs were evaluated during the course of this project. Several reports documenting findings were produced under this project. Namely:

1. Roger A. VanTassel, Wallace K. Wong, Signal-to-Noise Characteristics of Photodiode Array Fourier Transform Spectrometers, *Mikrochimica Acta [Wien]* 1988, II, 323-324.

Discusses the findings that the FAST interferometer is comparable in sensitivity to a single slit dispersive photodiode array spectrograph.

2. Roger A. VanTassel and Wallace K. Wong, Hadamard-Coded, Stationary-Entrance Mask, Photodiode-Array Spectrometer, in the SPIE Vol. 1145 (7th International Conference on Fourier Transform Spectroscopy), D.G. Cameron Ed., 1145, (1989) pp. 384-390.

Describes the Hadamard Transform Spectrometer concept which provides improved sensitivity over the original FAST concepts. Data processing algorithms were described along with preliminary computer simulated results.

3. U.S. Patent Number 5050989 was granted to Roger A. VanTassel and Wallace K. Wong for an invention known as Hadamard Spectrograph on 24 September 1991.

4. J. L. Robichaud, W. K. Wong, and R. V. VanTassel, Measured Performance of a Hadamard-coded Photodiode-Array Spectrometer, in the SPIE Vol. 1575 (8th International Conference on Fourier Transform Spectroscopy, H. M. Heise, E. H. Korte, and H. W. Siesler, Eds., (1992), pp. 255-257.

5. J. L. Robichaud, W. K. Wong, and R. V. VanTassel, Evaluation of a Hadamard-Coded Photodiode-array spectrometer under low illumination. The manuscript was submitted to Applied Optics, Optical Society of America in May, 1992 (accepted for publication).

## Signal-to-Noise Characteristics of Photodiode Array Fourier Transform Spectrometers

Roger A. Van Tassel<sup>1,\*</sup> and Wallace K. Wong<sup>2</sup>

<sup>1</sup> Air Force Geophysics Laboratory (LSP), Hanscom AFB, MA 01731, USA

<sup>2</sup> SSG, Inc., Waltham, MA 02154, USA

**Abstract.** The signal-to-noise characteristics of two configurations of photodiode array Fourier transform spectrometers are compared with that of a conventional grating spectrograph using an identical photodiode array. One configuration uses a Sagnac-type common path triangle interferometer, the other uses a stationary tilted mirror Michelson interferometer. While the common path triangle configuration has the property that the resolving power is independent of the field position, the  $S/N$  for both is reasonably comparable to the grating spectrograph.

**Key words:** photodiode array Fourier transform spectrometer.

Two configurations of photodiode array Fourier transform spectrometers which utilize techniques pioneered by Stroke and Funkhouser [1] to produce interferograms in space rather than in time have recently been described in the literature. One configuration uses a Sagnac-type common path triangle interferometer which shears an image of the source to produce two coherent sources which interfere when superimposed [2, 3]. These two coherent sources are then placed at the front focal plane of a Fourier transform lens with the detector array at the rear focal plane. A second configuration is based on a Michelson interferometer with a tilted rather than a moving mirror [4]. In this case the optical path difference is produced in the plane of the mirrors. The fringes are localized in this plane. They are then transferred to the detector array by means of a lens. The common path configuration has the property that the fringe spacing, and hence the resolving power, is independent of the field position, so that a large field-of-view is theoretically possible. To make use of this, however, requires an array with variable spacing along its length since the fringes will be spaced slightly more closely farther from the optical axis. The field limitations of

\* To whom correspondence should be addressed

the tilted mirror Michelson configuration are similar to that of a conventional scanning Michelson interferometer.

The signal on each detector element for an ideal instrument using either of these two configurations is given by

$$S_i = [2\epsilon\eta B_o \delta\sigma \Omega (A/n)] [1 + \cos 2\pi \sigma\Delta],$$

where  $\epsilon$  is the RT product of the beam splitter (0.25 for an ideal beam splitter),  $\eta$  is the instrument optical efficiency,  $B_o$  is the spectral radiance of the source,  $\delta\sigma$  is the bandwidth,  $\Omega$  is the field-of-view,  $A$  is the aperture and is equal to the total area of the detector array,  $n$  is the number of elements in the detector array, and  $\Delta$  is the optical path difference.

The signal of interest in signal-to-noise considerations, however, is the signal in spectral space which is given by the Fourier transform of the signals from the array of individual detector elements. This is given by

$$S = \text{FT}[S_i] = (n/\sqrt{2})(2\epsilon\eta B_o \delta\sigma \Omega a_i),$$

where  $A/n$  is replaced by  $a_i$ , the area of each individual detector element.

When the noise is pure detector noise, it is given by  $N_i = \text{NEP}_i/\sqrt{T}$ . Again, taking the Fourier transform to move into the spectral domain gives  $N = (\sqrt{n})\text{NEP}/\sqrt{T}$ . The signal-to-noise is given by

$$S/N = \sqrt{2n} (\epsilon\eta B_o \delta\sigma \Omega a_i \sqrt{T}) / (\text{NEP}_i).$$

This may be compared with the signal-to-noise using the same detector array in a grating spectrograph. In this case the signal is given by  $S_i = B_o \delta\sigma a_i \Omega \eta$ , where  $a_i$  is the area of the slit as well as the area of a single detector element and  $\Omega$  is the field of view of the instrument which is given by the area of the grating divided by the square of the focal length. The noise is the  $\text{NEP}/\sqrt{T}$ , so that

$$S/N(\text{spectrograph}) = (B_o \delta\sigma a_i \Omega \eta \sqrt{T}) / (\text{NEP}_i).$$

The ratio of the  $S/N$  of the Fourier spectrometer to that of a grating spectrograph using the same detector array and having the same field-of-view is then  $\sqrt{2n} \epsilon$ . For  $\epsilon = 0.25$  this ratio is approximately  $0.3\sqrt{n}$ , which for a 512 element detector works out to be a factor of eight. While this would appear to be a significant improvement over a grating spectrograph, it is a long way from the factors of a thousand associated with the performance of scanning Michelson interferometers over scanning grating spectrometers. In addition it is difficult to build a diode array Fourier spectrometer faster than about  $f/5$ , whereas  $f/2.5$  flat field spectrographs are presently available. This increase in optical speed makes the  $S/N$  for a diode array Fourier spectrometer reasonably comparable to a grating spectrograph fitted with the same array.

## References

- [1] G. W. Stroke, A. T. Funkhouser, *Phys. Lett.* 1965, 16, 272.
- [2] T. Okamoto, S. Kawata, S. Minami, *Appl. Opt.* 1984, 23, 269.
- [3] T. H. Barnes, *Appl. Opt.* 1985, 24, 3702.
- [4] H. Aryamanya-Mugisha, R. R. Williams, *Appl. Spectrosc.* 1985, 39, 693.

Received August 28, 1987.

Hadamard-Coded, Stationary-Entrance-Mask,  
Photodiode-Array Spectrometer

Roger A. Van Tassel  
Geophysics Laboratory, Hanscom AFB, Massachusetts 01731

Wallace K. Wong  
SSG, Inc., 150 Bear Hill Road, Waltham, Massachusetts 02154

ABSTRACT

A Hadamard transform spectrometer has been designed which uses a stationary Hadamard mask at the entrance plane of a holographic grating, photodiode array spectrometer. The mask contains  $2N-1$  slots where  $N$  is the number of resolution elements in the photodiode array. The instrument uses no moving parts and has the ability to capture the spectrum of a randomly occurring pulse source with significantly higher signal-to-noise ratio than a single-slit array spectrometer. It utilizes all-reflective optics and is a generic design suitable for use in the ultraviolet, visible and infrared when equipped with a detector array which is sensitive in the region of interest.

1. INTRODUCTION

Hadamard transform techniques are well known in spectroscopy and imaging to reduce the effects of detector noise.<sup>1</sup> In contrast to other Hadamard instrumentation which utilize moving masks, the design presented here uses a stationary Hadamard mask. The mask is placed at the entrance aperture of a dispersive array spectrometer. This design has three distinct advantages: 1) The optical throughput is increased substantially because on average, approximately  $N/2$  open slits will be imaged onto the detector array for each spectral resolution element, where  $N$  is the number of resolution elements or pixels in the detector array. 2) The design is inherently rugged because it does not require interferometric tolerances, and it has no moving parts, which avoids the difficulties which can arise from imperfections caused by motion of the mask. 3) It has the capability, as does a single-slit array spectrometer, of measuring the spectrum of randomly occurring pulse sources. The spectrum of a single pulse can be determined unambiguously even if the pulse length is less than the readout time of the array. Multiple pulses within the readout time are averaged.

2. COMPARISON WITH A SINGLE-SLIT ARRAY SPECTROGRAPH

Comparison of the Hadamard design with a conventional single-slit spectrometer which is equipped with a linear detector array is illustrated in Figure 1. Light enters the instrument through a single entrance slit. The optical separator disperses the radiation and, if the radiation is monochromatic, focuses an image of the slit on the focal plane. The location of this image is determined by the wavelength of the entering radiation. Multiple images are formed by polychromatic radiation and the spectrum is obtained directly from the output of the array after spectral calibration and correction for the gain and offset variations which are an inherent part of the data processing for linear photodiode arrays.

The following notation is introduced in this section because it is useful in describing the Hadamard design. As shown in Figure 2, in a single-slit spectrometer, radiation of wavelength  $l$ , expressed as  $(E_l)$ , falls on detector  $D_1$ ,  $E_2$  on  $D_2$ , etc. to  $E_7$  on  $D_7$ . An estimate of the energy  $E(n)$  is then given directly by the signal on the corresponding detector,  $D(n)$ . Typically the slit width is made identical to the width of the individual detector elements to obtain the highest spectral resolution. If a higher signal-to-noise ratio is needed, wider slits can be used, but the spectral resolution will be reduced.

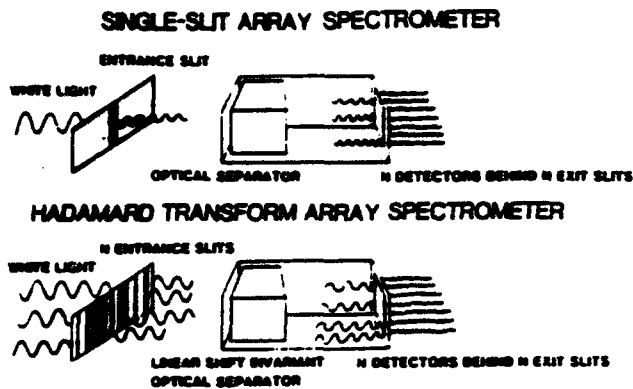


Figure 1. Comparison of a single-slit array spectrometer with a Hadamard-entrance-mask array spectrometer.

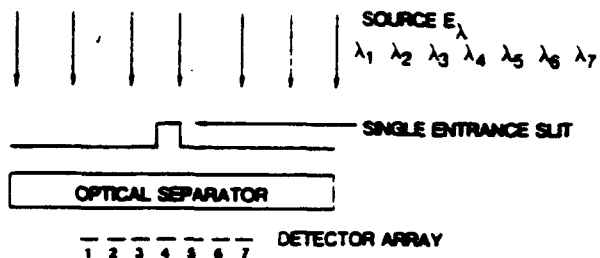


Figure 2. Optical schematic of a single-slit array spectrometer.

### 3. HADAMARD-MASK ARRAY SPECTROMETER

In the Hadamard design presented here, a Hadamard mask with  $2N-1$  slots is placed at the front focal plane of a spectrometer and is used as the entrance aperture for the system, as is shown in Figure 3. The pattern or coding of the Hadamard-mask is based on repeating the first row of an S-matrix. For monochromatic radiation a mirror image of the mask is then produced at the back focal plane by the optical separator. The position of this image is also determined by the wavelength of the incoming beam. For polychromatic radiation, multiple images are superimposed on the detector array.

#### 3.1 Formation of the S-matrix

Initially we assume that the optical system is perfect. This means that a mirror image of the mask is reproduced perfectly at the exit plane. In addition, we assume that it is linear shift invariant so that a change in the wavelength of the incoming radiation by  $n \delta\lambda$  will shift the image of the mask exactly  $n$  pixels, where  $n$  is an integer from 1 to  $N$ , the total number of resolution elements, and  $\delta\lambda$  is the spectral bandwidth or resolution.

For  $N = 7$ , there are 13 individual slits. These are denoted by  $S_1, S_2 \dots S_{13}$ . The wavelengths are defined to be the same as those for a single-slit spectrometer, i.e. radiation from the central slit falling on detector  $D_1$  is  $E_1$ . Radiation of central wavelength ( $E_4$ ) passing through position  $S_7$  appears at the position of detector  $D_4$ . Because this image is reversed by the imaging optics, the energy from position  $S_8$  appears at  $D_3$ ,  $S_9$  at  $D_2$ , and  $S_{10}$  at  $D_1$ , while radiation from  $S_{11}, 12 \& 13$  falls out of the field of the entire array.

This procedure results in the following set of equations which indicate the combinations of wavelengths which contribute to the signal from the different detector elements:

$$\begin{aligned}
 D_7 &= E_1 + E_2 + E_3 + E_5 + e_1 \\
 D_6 &= E_1 + E_2 + E_4 + E_7 + e_2 \\
 D_5 &= E_1 + E_3 + E_6 + E_7 + e_3 \\
 D_4 &= E_2 + E_5 + E_6 + E_7 + e_4 \\
 D_3 &= E_1 + E_4 + E_5 + E_6 + e_5 \\
 D_2 &= E_3 + E_4 + E_5 + E_7 + e_6 \\
 D_1 &= E_2 + E_3 + E_4 + E_6 + e_7
 \end{aligned}$$

where  $e(n)$  is the noise associated with each of the detector elements.

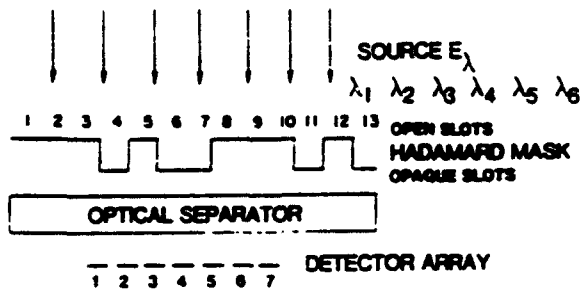


Figure 3. Optical schematic of a Hadamard-entrance-mask array spectrometer.

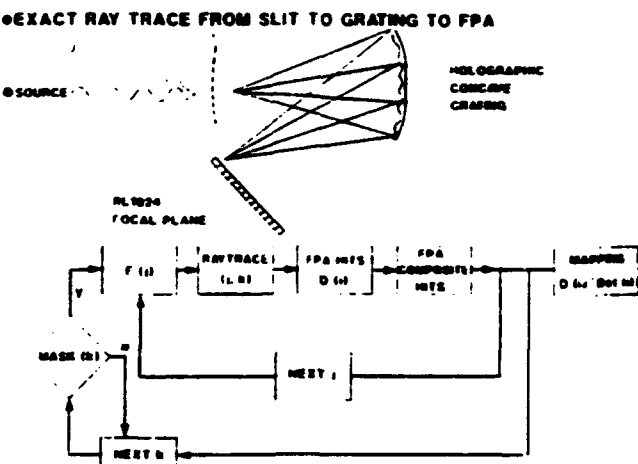


Figure 4. Schematic of the ray-tracing procedure used to determine the weighting matrix,  $W$ .

These equations can be expressed in matrix notation as  $D_r = S E + e$ , where  $D_r$  is the signal from the detector elements, with the subscript  $r$  used as a reminder that the elements must be read in reverse because the image is reversed, and  $S$  is an  $S$ -matrix of order 7 given by

$$S = \begin{vmatrix} 1 & 1 & 1 & 0 & 1 & 0 & 0 \\ 1 & 1 & 0 & 1 & 0 & 0 & 1 \\ 1 & 0 & 1 & 0 & 0 & 1 & 1 \\ 0 & 1 & 0 & 0 & 1 & 1 & 1 \\ 1 & 0 & 0 & 1 & 1 & 1 & 0 \\ 0 & 0 & 1 & 1 & 1 & 0 & 1 \\ 0 & 1 & 1 & 1 & 0 & 1 & 0 \end{vmatrix}$$

Notice that the first row of this matrix is given by the first seven slits of the mask. Because the S-matrix is a left circulant matrix, the remainder of the matrix may be found by shifting one place to the left while moving down a row.

The source spectrum is estimated by multiplying  $D$  by the inverse of the  $S$ -matrix,  $E = S^{-1}D + S^{-1}e$ . The source spectrum is given by the first term,  $E = S^{-1}D$ , and the noise by  $E - E = S^{-1}e = (\sqrt{N}/2)e$ , where  $N$  is the number of elements in the detector array and  $e$  is the average noise of a single detector element.

### 3.2 Effect of optical aberration and anamorphic magnification

The above formulation assumed perfect imaging of the individual slits of the Hadamard mask on the individual elements of the detector array for all wavelengths. However, optical aberrations will cause limitations on the quality of this image. In addition, we have assumed that the image of the entire mask is shifted linearly for a shift in wavelength, e.g. that slits 1,2,3,...at the entrance mask are imaged respectively unto elements  $j+1, j+2, j+3, \dots$  at the detector plane. Deviation from this condition is called anamorphic magnification.

When the effects of optical aberration and anamorphic magnification are included in the analysis, the energy distribution at the detector array may be given as  $D = WS + e$ , where  $W$  is a matrix containing the actual weighting coefficients. The matrix,  $W$ , may be expressed as the product of  $S$  and  $T$ , such that  $W = ST$ , where  $S$  is the simplex matrix of 1's and 0's, and  $T$  becomes the transfer matrix which represents the difference between the real system and an idealized system. For a perfect optical system  $T$  is an identity matrix of order  $N$ ; for any practical system it will approximate a diagonal matrix.

#### 4. SIMULATION OF THE PRELIMINARY HADAMARD DESIGN

The performance of a preliminary Hadamard-mask array spectrometer was assessed by modeling a system using an array with 167 elements. An f/2 flat-field spectrograph monochromator was designed by American Holographic of Littleton, Massachusetts, specifically for this application. The design uses a single, concave, holographic grating and places the Hadamard mask on the front focal plane, which is curved to improve the focus on the detector array. This particular design assumes that the detector array is flat, although it is possible to specify a curved detector array as well. This would allow both the entrance mask and detector array to lie on a Rowland circle.

The W-matrix was determined by means of a ray-tracing program. The procedure is represented diagrammatically in Figure 4. Rays were traced for each of the 167 wavelengths from each of the 167 open slots on the mask to 81 different places on the grating and were then propagated to an element on the detector plane.

##### 4.1 Simulation for a noise-free detector

Two different types of spectra were used to assess the design, a spectrum consisting of a ramp with intensity one at wavelength 1 to intensity 167 at wavelength 167, and a spectrum consisting of only a single line. The spectra were then recovered in two ways to assess the impact of optical aberrations and anamorphic magnification. The designation "uncorrected spectra" refers to a procedure in which the spectrum is recovered using only the inverse of the S-matrix. This ignores the effects of optical aberrations. The corrected spectrum uses the full W-matrix and includes corrections for all optical aberrations.

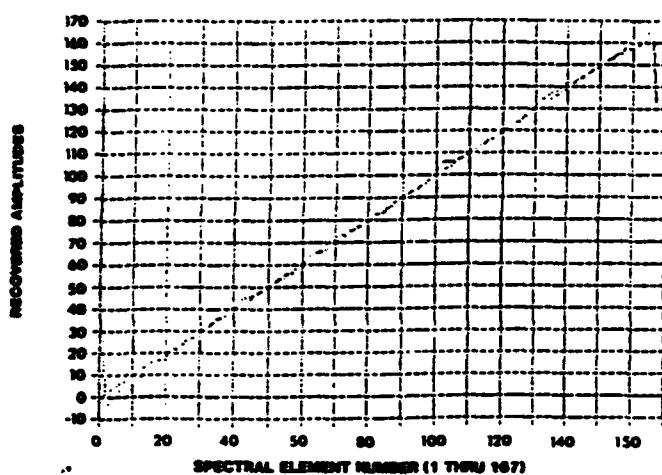


Figure 5. Recovered spectra of a ramp input spectrum using the inverse of the S matrix (uncorrected) and the inverse of the W matrix (corrected).

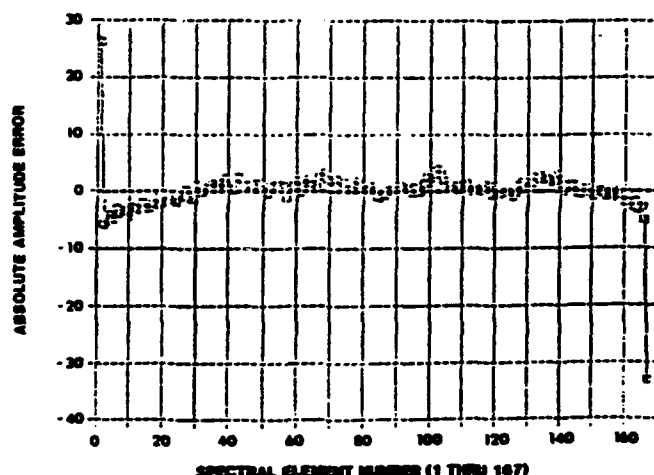


Figure 6. Absolute amplitude error of the uncorrected spectrum depicted in Figure 5.

The results of using both procedures with the ramp spectrum as the input are shown in Figure 5 with the errors plotted in Figures 6 and 7. Significant errors occur using only the S-matrix, especially at the ends of the spectral range. These are largely corrected when the T-matrix is included. As can be seen in Figure 7, the absolute deviations increase as the signal increases.

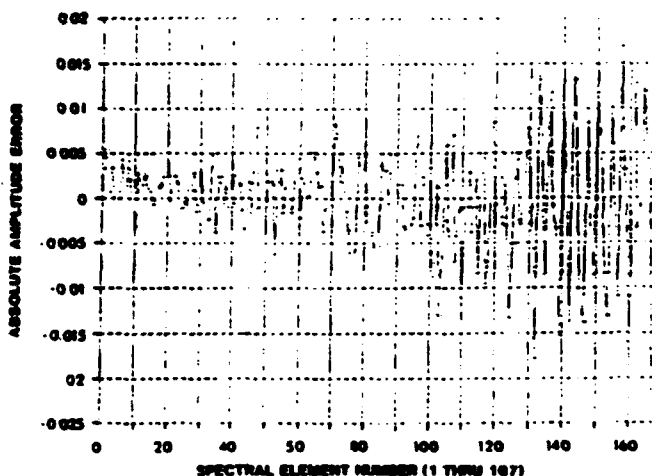


Figure 7. Absolute amplitude error of the corrected spectrum depicted in Figure 5.

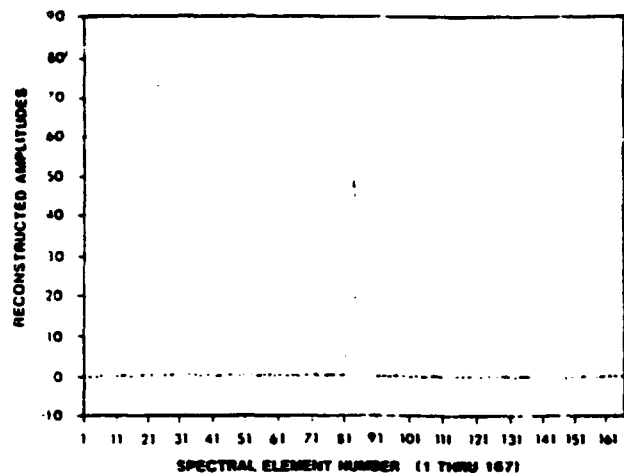


Figure 8. Recovered uncorrected spectrum of a line input spectrum at E81 with amplitude of 81.

The same procedure was used with a source spectrum consisting of a single line of intensity 81 at E81. The recovered uncorrected spectrum using only the S-matrix is shown in Figure 8, with the amplitude errors plotted in Figure 9. The recovered corrected spectrum using both the S- and T-matrix is shown in Figure 10, with its amplitude errors plotted in Figure 11. The recovered line spectrum is broadened significantly if only the S-matrix is used to determine the spectrum. Using both S- and T-matrices reduces these errors to insignificance.

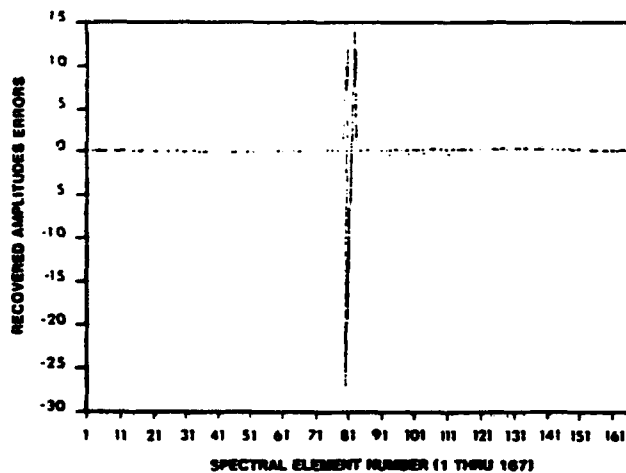


Figure 9. Absolute amplitude error of the spectrum shown in Figure 8.

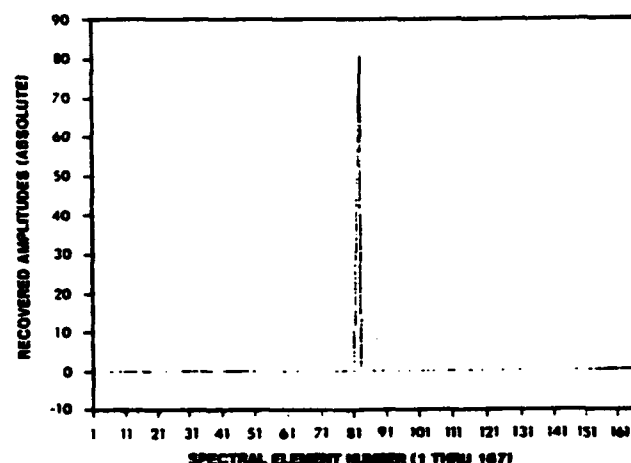


Figure 10. Recovered corrected spectrum of a line input spectrum at E81 with amplitude of 81.

#### 4.2 The effects of detector noise

The effects of noise were assessed by using actual noise which had been recorded from a Reticon 1024S photodiode array. A sample of dark noise with a single line superimposed at E88 is shown in Figure 12. The amplitude of the line was chosen to be three times the rms detector noise. This is the output which may be expected from a single-slit array spectrometer. At this level the line is obscured by detector noise.

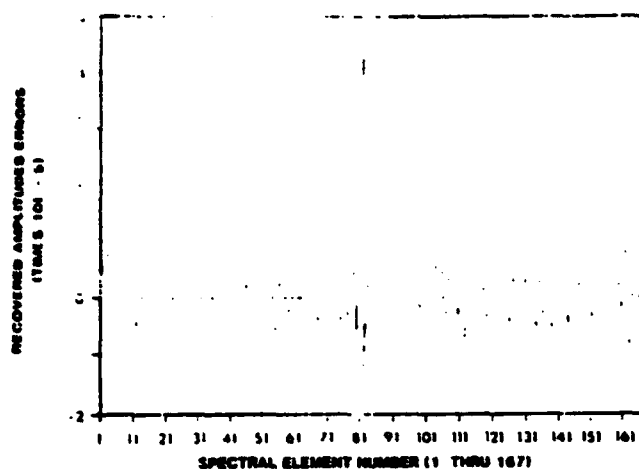


Figure 11. Absolute amplitude error of the spectrum shown in Figure 10.

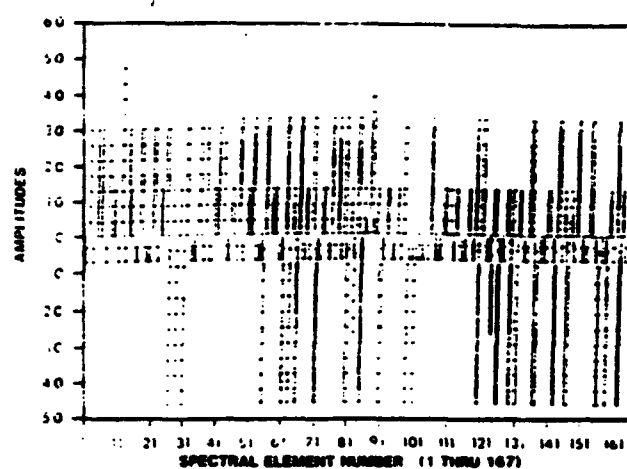


Figure 12. The output of a single-slit, array spectrometer with detector noise from a Reticon photodiode array superimposed over a spectral line at E81 with a S/N of approximately 3.

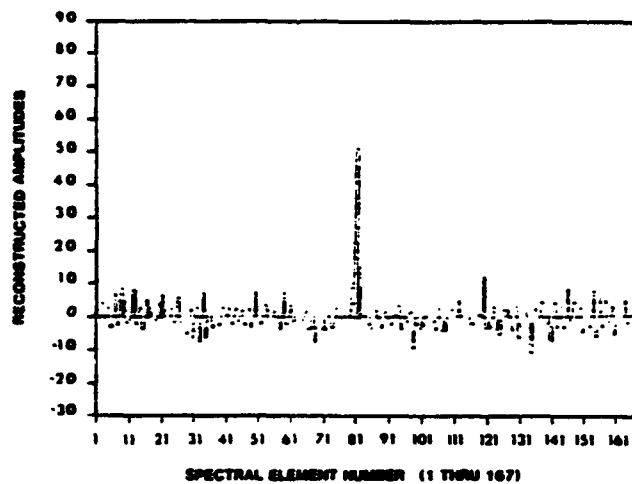


Figure 13. The uncorrected recovered spectrum with a line at E81 having an amplitude identical to that in Figure 12.

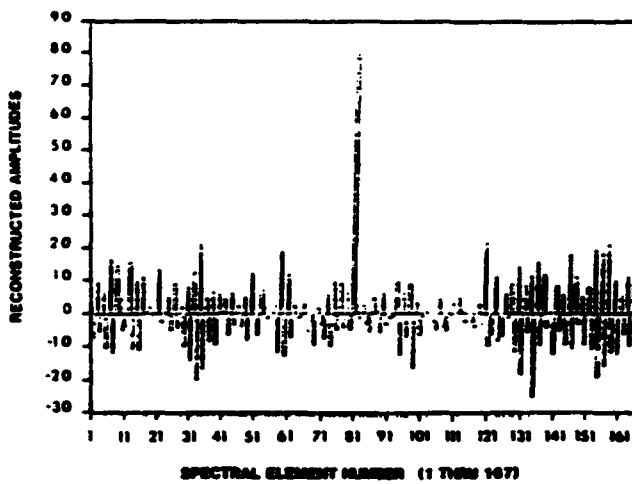


Figure 14. The corrected recovered spectrum with a line at E81 having an amplitude identical to that in Figure 12.

Using a source spectrum consisting of the same amplitude at E81 in the Hadamard system demonstrates the ability of this system to significantly improve the signal-to-noise ratio. Figures 13 and 14 show the uncorrected and corrected spectra, respectively. The amplitude error of the line is lower in the corrected spectrum, although the noise in this spectrum is greater.

##### 5. CONCLUSIONS

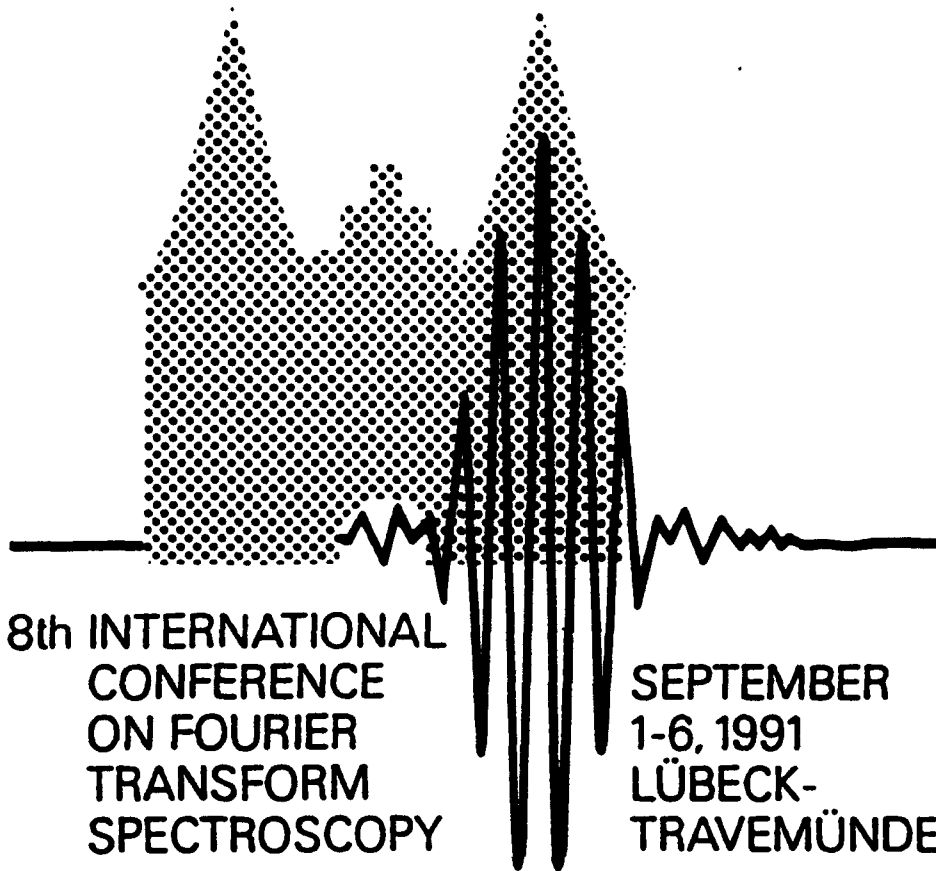
An analysis of a preliminary design of a photodiode-array, grating spectrometer with an entrance aperture widened by means of a Hadamard mask demonstrates that this concept is useful for significantly increasing the signal-to-noise over that of a conventional array spectrometer.

#### 6. ACKNOWLEDGMENTS

The authors wish to thank Tom Mikes of American Holographic, Littleton, MA, for the preliminary design of the flat-field, holographic, concave-grating monochromator, as well as for providing a copy of the ray-tracing program, and Stephan Davis of Real Time Engineering, Inc., Holliston, MA, for the software development. Wallace Wong was supported under Air Force Contract F19628-85-C-0103.

#### 7. REFERENCES

1. M. Harwit and N.J.A. Sloane, Hadamard Transform Optics, Academic Press, New York (1979).



8th INTERNATIONAL  
CONFERENCE  
ON FOURIER  
TRANSFORM  
SPECTROSCOPY

SEPTEMBER  
1-6, 1991  
LÜBECK-  
TRAVEMÜNDE

*Proceedings Editors:*

**H. M. Heise  
E. H. Korte  
H. W. Siesler**

*Sponsor:*

**DASp—Deutscher Arbeitskreis für Angewandte Spektroskopie  
in der Fachgruppe Analytische Chemie  
der Gesellschaft Deutscher Chemiker (GDCh)**

*Cooperating Organizations:*

**ISAS—Institut für Spektrochemie und angewandte Spektroskopie  
SPIE—The International Society for Optical Engineering**

**SPIE Volume 1575**

## Measured Performance of a Hadamard-coded Photodiode-array Spectrometer.

Joseph L. Robichaud  
OSS, Inc., 50 Dalton St, Tewksbury, MA 01876

Wallace K. Wong  
SSG, Inc., 150 Bear Hill Rd, Waltham, MA 02154

Roger A. Van Tassel  
Philips Laboratory (GP/OPS), Hanscom AFB, MA 01731

### ABSTRACT

We report performance measurements of a photodiode array Hadamard transform spectrometer (HTS) with a stationary entrance mask. The high throughput of the multi-slit, no-moving parts instrument is shown to yield a significantly higher S/N ratio than a single-slit array spectrometer. In addition, we examine sources of instrument noise and propose techniques to further enhance system performance.

### 1. INTRODUCTION

The application of Hadamard transform techniques in spectroscopy has provided throughput and/or multiplexing advantages in comparison with traditional single-slit spectrometers<sup>1,2</sup>. A single slit spectrometer can capture all of the spectral components simultaneously by the addition of a photodiode array in the exit plane. However, the throughput of the instrument is still severely limited by the small area of the entrance aperture.

Improved throughput has been obtained by application of large area spatially encoded masks at the entrance and/or exit planes. However, a doubly encoded instrument with  $N$  entrance and  $N$  exit slots required  $2N-1$  measurements<sup>3</sup>. More recently a no-moving parts, Hadamard coded entrance mask, photodiode array instrument has been proposed<sup>4</sup>. The instrument has a throughput advantage over a traditional single slit spectrometer since approximately  $N/2$  open slits are used to image radiation onto the detector array. The design requires no interferometric tolerances, and, having no moving parts, it is inherently more rugged than a scanning system. Additionally, the spectrometer measures all the spectral elements simultaneously, providing the capability of measuring randomly occurring pulse sources.

### 2. INSTRUMENTATION AND EXPERIMENTAL PROCEDURES

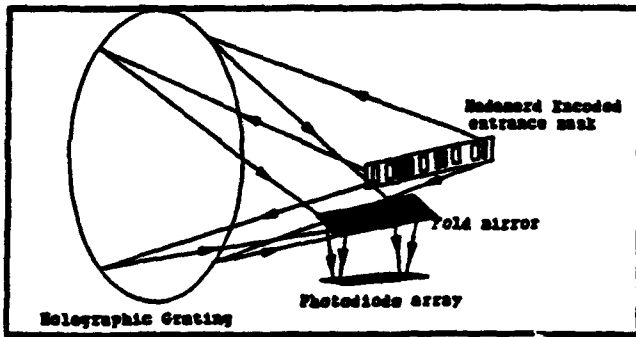


Figure 1: Optical Schematic

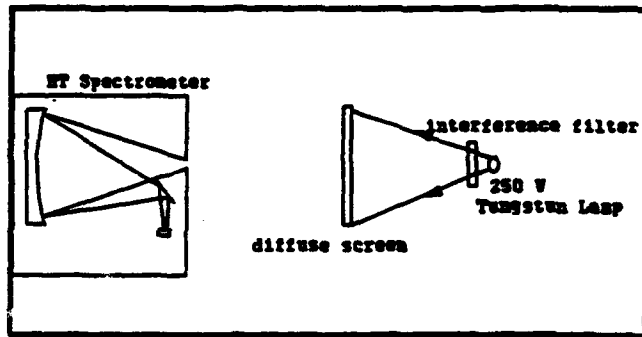


Figure 2: Experimental Arrangement

An optical schematic of the system is shown in Figure 1. Construction of the instrument was based on an F/2, 300 mm radius of curvature holographic grating. The entrance mask is comprised of 1005 adjoining slots, each slot 50  $\mu$ m wide by 3.0 mm high. The spatial encodement of the entrance mask is based on an  $N=503$  Hadamard

encodement. The detector array is an EG&G RL1024SAF silicon photodiode array, consisting of 1024 photodiodes, each  $25\text{ }\mu\text{m}$  by  $2.5\text{ mm}$  large. The system has a spectral range of  $622\text{ nm}$  to  $1072\text{ nm}$  with a resolution of  $0.9\text{ nm}$ .

In our experimental arrangement (Figure 2) a  $250\text{ W}$  white light Tungsten lamp was filtered by an  $840\text{ nm}$  ( $13\text{ nm}$  FWHM) interference filter and used to illuminate a diffuse transmitting screen in front of the spectrometer's entrance mask. The size of the illuminated area was controlled to create an  $F/2$  object.

The adjacent diodes in the 1024 array were summed to form an equivalent 512 pixel array. A segment which corresponded to a 503 element sample was selected from the 512 data points after calibration with a monochromatic source (HeNe laser). Further preprocessing consisted of removal of the dark voltage detector noise. The dark voltage was obtained by blocking the entrance mask and taking a detector output voltage file. The data was then multiplied by an inverse S-matrix in order to decode the Hadamard encoded spectral information.<sup>8</sup>

### 3. DATA ANALYSIS

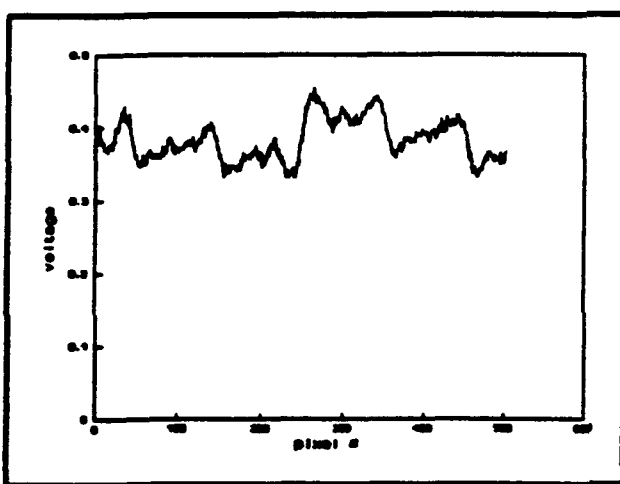


Figure 3: Detector Output

The detector output obtained is presented in Figure 3. Each spectral element passing through the entrance mask has created a shifted and superimposed image of the mask at the focal plane. The spectrum resulting from transformation of the detector voltage pattern is presented in Figure 4. The S/N ratio has been measured as 12.7. Additionally, the prominent peak occurs at  $839.7\text{ nm}$  with a FWHM of  $14.1\text{ nm}$ , which agrees with the transmission properties of the interference filter used within our experimental error. By masking off all but one of the  $50\text{ }\mu\text{m}$  entrance slits in the entrance mask the multislit spectra was easily compared with the result from a single slit spectrometer. The detector output obtained in the single slit configuration is presented in Figure 5, here we measure a S/N ratio of 2.2. The throughput advantage in the multislit configuration has improved the instrument's S/N ratio by a factor of 5.7.

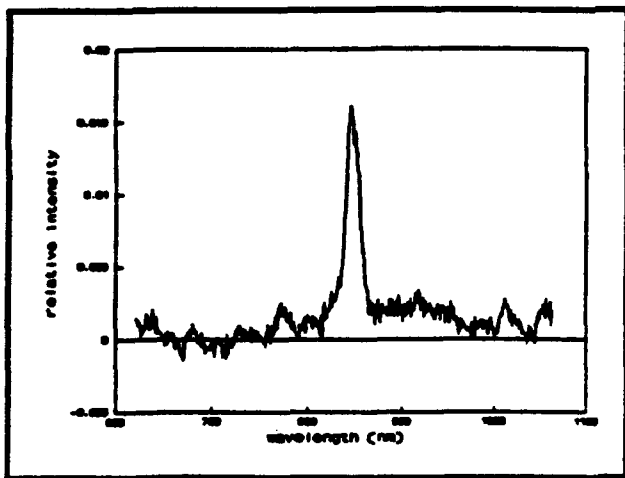


Figure 4: Multislit Spectrum

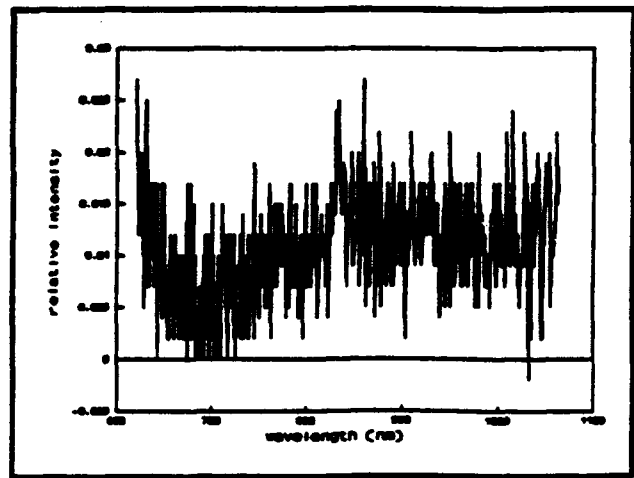


Figure 5: Single Slit Spectrum

#### 4. CONCLUSIONS AND SUGGESTIONS

The constructed Hadamard Transform spectrometer has displayed the capability of simultaneously capturing spatially encoded spectral information. The encoded spectrum of an 840 nm test source has been successfully reconstructed utilizing the instrument's throughput advantage to yield a S/N improvement of almost a factor of 6 in comparison to a single slit configuration. This improved S/N performance is not as high as the theoretical limit of  $N^{1/2}/2 = 11$  due partially to unrealized assumptions in our theoretical model<sup>4</sup>. Our theoretical model decodes spectral information from the spatially encoded voltage output by transformation through a binary S-matrix, using matrix elements of 1's and 0's exclusively. The binary S-matrix assumed perfect optical imaging, linear shift invariance, and uniform detector and grating efficiencies. A truer representation of our system, and a better decoding scheme, could be implemented by replacing the binary S-matrix with a W-matrix which contains the actual weighting coefficients corresponding to our instrument's imaging and dispersion properties and its spectral responsivities<sup>4</sup>.

#### 5. ACKNOWLEDGEMENTS

The authors wish to thank Tom Mikes and Charles Hatch of American Holographic, Littleton, Ma, for design of the grating and construction of the instrument, and also Stephen Davis of Real Time Engineering, Inc., Holliston, Ma, for the software development.

#### 6. REFERENCES

1. J.A. Decker Jr, 'Experimental Realization of the Multiplex Advantage with a Hadamard Transform Spectrometer', *Appl. Opt.* 10, 510, 1971.
2. M.J.E. Golay, 'Multi-slit Spectrometry', *J. Opt. Soc. Am.* 39, 437, 1949; 'Static Multislit Spectrometry and its application to the Panoramic Display of Infrared Spectra', *J. Opt. Soc. Am.* 41, 468 (1951).
3. N.J.A. Sloane, 'Reducing the Number of Measurements in Doubly Multiplexed Spectrometers', *Aspen Int. Conf. on Fourier Spectroscopy* (G.A. Vanasse, A.T. Stair, D.J. Baker, Eds.), 1970.
4. R.A. Van Tassel, W.K. Wong, 'Hadamard-Coded, Stationary-Entrance-Mask, Photodiode-Array Spectrometer', *7th International Conference on Fourier Transform Spectroscopy*, 1145, 384, 1989.
5. M. Harwit, N.J.A. Sloane, *Hadamard Transform Optics*, Academic Press, New York N.Y., 1979.

**Evaluation of a Hadamard-coded photodiode-array Spectrometer  
under low illumination**

**Joseph L. Robichaud**

**OSS, Inc., 50 Dalton St, Tewksbury, MA 01876**

**Wallace K. Wong**

**SSG, Inc., 150 Bear Hill Rd, Waltham, MA 02154**

**Roger A. Van Tassel**

**Geophysics Directorate, Phillips Laboratory (PL/GPOS),  
Hanscom AFB, MA 01731**

**ABSTRACT**

Hadamard spectrometers are well known for their multiplexing and/or throughput advantages. Traditionally these instruments require moving entrance and/or exit masks. The performance of a breadboard photodiode-array Hadamard transform spectrometer (HTS) with a stationary entrance mask was evaluated against the same instrument configured with a single entrance slit. The higher throughput of the multislit, no-moving parts instrument has provided a higher signal to noise ratio (S/N) over the single slit spectrometer under low illumination conditions. Sources of noise are examined for the single slit and multislit Hadamard instruments and improvements for future designs suggested.

**keywords:** Hadamard transform, spectroscopy, high throughput.

## I. INTRODUCTION

The application of Hadamard transform techniques in spectroscopy has provided throughput and/or multiplexing advantages in comparison with traditional single slit spectrometers.<sup>1,2</sup> A single slit spectrometer can capture all of the spectral components simultaneously by the use of a photodiode-array in the exit plane. However, the throughput of the instrument is still severely limited by the small area of the entrance aperture.

Improved throughput has been obtained by application of large area, spatially encoded masks at the entrance and/or exit planes. These multislit instruments use a single detector and moving entrance or exit masks. Doubly encoded designs with  $N$  entrance and  $N$  exit slits require  $2N-1$  measurements.<sup>3</sup> More recently a Hadamard-coded entrance mask, photodiode-array instrument has been proposed and demonstrated, it has the advantage of no moving parts.<sup>4,5</sup> The instrument has a theoretical throughput advantage over a traditional single slit spectrometer since approximately  $N/2$  open slits are used to image radiation onto the detector array. The design does not require interferometric tolerances, and, having no moving parts, it is inherently more rugged than a scanning system. Additionally, the spectrometer measures all the spectral elements simultaneously, providing the capability of measuring randomly occurring pulse

sources.

### III. THEORETICAL COMPARISON WITH SINGLE SLIT SPECTROMETER

Comparison of the Hadamard design with a conventional single slit, photodiode-array spectrometer is illustrated in Figure 1. The single slit spectrometer will be described in order to introduce notation which is useful in describing the Hadamard design.

#### **A. Single Slit Photodiode-array Spectrometer.**

In the single entrance slit instrument the optical separator disperses the incoming radiation and forms an image of the entrance slit at the focal plane. The location of this image is determined by the wavelength of the incoming radiation. Multiple images are formed by polychromatic radiation, and the spectrum is obtained directly from the output of the array. An estimate of the energy  $E(n)$  is given directly by the signal on the corresponding detector  $D(n)$ , by

$$D(n) = E(n) + e(n), \quad (1)$$

where  $n$  is an index over the number of spectral elements,  $N$ , and  $e(n)$  is the detector noise associated with the  $n$ th detector. In this single slit instrument the energy of the  $n$ th spectral element is estimated by

$$\langle E(n) \rangle = D(n), \quad (2)$$

and the difference between the estimate and the energy is

$$\langle E(n) \rangle - E(n) = e(n). \quad (3)$$

We can use equation (3) to form an expression for the theoretical signal to noise ratio expected from the single slit spectrometer as

$$S/N_{\text{single slit}} = E(n)/e(n). \quad (4)$$

#### **B. Hadamard Transform Photodiode-array Spectrometer.**

In the Hadamard design presented here, a Hadamard mask with  $2N-1$  slits is placed at the front focal plane of a spectrometer and is used as the entrance aperture for the system. The pattern, or coding, of the Hadamard mask is based on repeating the first row of a circulant S-matrix, as well described by Harwit and Sloane.<sup>6</sup> For monochromatic radiation a mirror image of the mask is produced at the back focal plane. The position of this image is determined by the wavelength of the incoming beam. For polychromatic radiation, multiple images are superimposed on the detector array. We can form a general expression for the detector output,

$$D(n) = e(n) + \sum_{j=0}^{N-1} E(j+1) * S[j+N-(n-1)], \quad (5)$$

where  $j$  is an index over the  $N$  spectral elements and  $S(j)$  represents the encodement of the  $2N-1$  slit positions.

For illustration we consider the case of  $N=7$ . For  $N=7$ , there are 13 individual slits. We model an idealized optical system where a mirror image of the entrance mask is perfectly reproduced at the exit plane. In addition, we assume that the instrument is linear shift invariant so that a change in wavelength of the incoming radiation by  $m\delta\lambda$  will shift the image of the mask by exactly  $m$  pixels, where  $m$  is an integer from 1 to  $N$ . We can apply equation (5) to this idealized instrument along with the Hadamard encodement,<sup>6</sup>

$$1 \ 1 \ 1 \ 0 \ 1 \ 0 \ 0 \ 1 \ 1 \ 1 \ 0 \ 1 \ 0, \quad (6)$$

where 1 represents a transmitting slit position and 0 an opaque slit position, to yield a specific set of equations representing the 7 detector outputs as

$$\begin{aligned} D(1) &= E(2) + E(3) + E(4) + E(6) + e(1) \\ D(2) &= E(3) + E(4) + E(5) + E(7) + e(2) \\ D(3) &= E(1) + E(4) + E(5) + E(6) + e(3) \\ D(4) &= E(2) + E(5) + E(6) + E(7) + e(4) \\ D(5) &= E(1) + E(3) + E(6) + E(7) + e(5) \\ D(6) &= E(1) + E(2) + E(4) + E(7) + e(6) \\ D(7) &= E(1) + E(2) + E(3) + E(5) + e(7). \end{aligned} \quad (7)$$

We can express the detector outputs in matrix form by

$$D_n = S E_n + e_n, \quad (8)$$

where  $S$  is an S-matrix of order 7 given by,

$$S = \begin{bmatrix} 1 & 1 & 1 & 0 & 1 & 0 & 0 \\ 1 & 1 & 0 & 1 & 0 & 0 & 1 \\ 1 & 0 & 1 & 0 & 0 & 1 & 1 \\ 0 & 1 & 0 & 0 & 1 & 1 & 1 \\ 1 & 0 & 0 & 1 & 1 & 1 & 0 \\ 0 & 0 & 1 & 1 & 1 & 0 & 1 \\ 0 & 1 & 1 & 1 & 0 & 1 & 0 \end{bmatrix}. \quad (9)$$

We can find an estimate for the energy,  $\langle E_n \rangle$ , by

$$E_n = S^{-1}(D_n - e_n), \quad (10)$$

$$\langle E_n \rangle = S^{-1}D_n, \quad (11)$$

in this case estimating the energy of the spectrum requires matrix multiplication by an inverse S-matrix. The difference between the estimate and the energy is given by,

$$(E_n) - E_n = S^{-1}e_n = \sqrt{N}e, \quad (12)$$

where  $N$  is the number of spectral elements and  $e$  is the average noise of a single detector element.<sup>6</sup> We can use equation (12) to form an expression for the theoretical signal to noise ratio expected from the multislit spectrometer as

$$S/N_{\text{multislit}} = ((N/2) * E_n) / e_n. \quad (13)$$

The factor of  $N/2$  is a result of the  $N/2$  open slits which are

used to image radiation onto the detector array. We can determine the theoretical S/N ratio improvement obtained with the multislit instrument by taking the ratio of the single slit and multislit S/N ratios from equations (4) and (13),

$$\frac{(S/N)_{\text{multi}}}{(S/N)_{\text{single slit}}} = \frac{\frac{N/2 * E}{\sqrt{N * e}}}{\frac{E}{e}} = \frac{\sqrt{N}}{2}. \quad (14)$$

The above formulation assumed perfect imaging of the entrance mask onto the focal plane for all wavelengths. However, optical aberrations will cause limitations on the quality of the image. The degree of aberration will vary for different wavelengths, since different wavelengths are imaged onto the detector array from different entrance mask slit positions. In addition, we have assumed a shift invariant system. Anamorphic magnification in a real instrument will cause deviation from our theoretical construction. When the effects of optical aberration and anamorphic magnification are included in the analysis, the energy distribution at the detector array may be given as

$$D_n = W E_n + e_n \quad (15)$$

where  $W$  is a matrix containing the actual weighting coefficients corresponding to the real instrument.<sup>6</sup>

### III. INSTRUMENTATION AND EXPERIMENTAL ARRANGEMENT

A photograph of the instrument is shown in Figure 2. Construction of the instrument was based on an  $F/2$ , 300 mm radius-of-curvature, holographic grating. The entrance mask is comprised of 501 adjoining slit positions, each  $50 \mu\text{m}$  wide by 1.5 mm high. The spatial encodement of the entrance mask is based on an  $N=251$  Hadamard encodement. The detector array is an EG&G RL1024SAF silicon photodiode-array, consisting of 1024 photodiodes, each  $25 \mu\text{m}$  wide by 2.5 mm high. The system has a spectral range of 737 nm to 953 nm with a theoretical resolution of 0.9 nm. The grating was designed on a Rowland circle.<sup>7</sup> The entrance mask was formed on a flexible film to allow for the required curvature while a curved focal plane was achieved by a concave spherical fiber optic face plate. The integration time of the detector array was set at 180 ms. Array readout was implemented with a Keithley A-D converter in an IBM-AT personal computer.

The experimental arrangement is presented in Figure 3. A variable power Tungsten lamp was filtered by a 806 nm (13 nm FWHM) interference filter and used to illuminate a diffuse transmitting screen in front of the spectrometer's entrance mask. The size of the illuminated area was controlled to match the acceptance angle of the spectrometer.

Adjacent diodes in the 1024 array were summed to form an equivalent 512 pixel array. A segment which corresponded to a 251 element sample was selected from the 512 data points after calibration with a Xe pen lamp line source. Further preprocessing consisted of removal of the detector dark voltage. The dark voltage was obtained by blocking the entrance mask and taking a detector output voltage file. The data were then multiplied by an inverse S-matrix in order to decode the Hadamard encoded spectral information.

A Xe pen lamp was used for absolute wavelength calibration and also to determine the spectral resolution. The pen lamp is constructed from 6 mm diameter quartz tubing, and is 50 mm in length. This shape allowed us to locate the lamp directly in front of the entrance mask in a horizontal orientation, providing relatively uniform illumination across the entrance mask. We insured that all of the instrument's acceptance angle was used by inserting a diffuser between the lamp and the entrance mask.

#### IV. DATA AND ANALYSIS

##### **A. Xe Pen Lamp Source.**

Spectra obtained from the Xe pen lamp in single and multislit configurations are presented in Figures 4 and 5. Analysis of the strong line at 883 nm the Hadamard transformed spectra yields a spectral line width of 2.5 nm. The single slit

spectra yields a line width of 2.4 nm for the same line, however, this spectral width was obtained with a 100  $\mu\text{m}$  slit width, as opposed to the 50  $\mu\text{m}$  slit widths used in the multislit mask. This apparent loss of resolution with the multislit mask may be attributed to the optical aberration of the imaging properties of the concave holographic grating. The instrument requires imaging of a 25 mm object with uniform dispersion, magnification, and blur size. Any deviation from perfect optical performance results in a reconstructed spectra with noise broadened spectral features.

#### *B. Narrow Bandpass Filter Source.*

The data taken with the narrow bandpass filtered source yielded detector outputs as displayed in Figure 6. This detector output, or encodegram, is a result of the superposition of many images of the Hadamard encoded entrance mask at the focal plane. A number of reconstructed spectra obtained with different illumination levels are presented in Figure 7. The spectral features long of the peak centered at 806 nm are instrumental artifacts. The single slit (100  $\mu\text{m}$ ) spectra were obtained directly from the detector output after replacing the multislit entrance mask with a single slit entrance mask. The single slit spectra obtained with the same three illumination levels are presented in Figure 8.

#### *C. Noise Sources.*

A comparison of the single and multislit spectra shows that the spectral noise in the two instruments has different characteristics. The single slit spectra has a noise distribution which appears to be relatively constant as the source strength is increased. However, the noise in the multislit spectra increases with the source strength. This observation is quantified in Figure 9 where the 100  $\mu\text{m}$  single slit (b) and 50  $\mu\text{m}$  Hadamard encoded multislit (a) instruments have been used to obtain a number of different S/N ratios versus source strength. The source strength was measured with a Si photodiode on a relocatable stage. The single slit S/N increases linearly with source strength for the full range of source levels examined. The multislit spectra S/N increases with source strength at a faster rate than the single slit spectra but then levels off at a S/N ratio of approximately 18. The single slit spectra S/N improves linearly since the main source of noise is detector noise which is relatively constant. The dark voltage of the detector array was obtained and removed from each of the detector output files. However, the dark voltage was found to fluctuate with time. It is this dark voltage fluctuation which represents the main source of noise in the single slit detector instrument.

Under low illumination levels this dark voltage fluctuation is the dominant source of noise for the multislit instrument and accordingly the multislit instrument S/N ratio increases as the

source strength increases and overcomes the dark voltage variation. In source strength regions above  $70 \mu\text{W}/\text{m}^2$  another noise mechanism begins to dominate and limits the HTS S/N. The spectral noise begins to increase proportionally with the peak signal strength. This noise can be attributed predominately to optical aberrations.

Systematic errors in the instrument can be thought of as encodegram error. A number of mechanisms exist which will cause the encodegrams to deviate from the idealized imaging assumed in our theoretical analysis. The layout of the instrument demands off-axis imaging of the entrance mask. This results in non-uniform blurring for different portions of the mask which varies with wavelength, since different portions of the entrance mask are used for different wavelengths. Additionally, anamorphic magnification and stray light are other noise sources which will be correlated with the encodegram, and therefore with the wavelength of the test source. The strength of these encodegram errors increases as the source strength increases. They eventually limit the Hadamard transform spectrometer application in strong illumination level situations.

The effect of the detector dark noise fluctuation on the spectra has been determined by sampling 100 dark voltage outputs. One output file has been subtracted from the others to yield 99 files which contain information about the detector array dark

voltage variation with time. The average value of the standard deviation of each detector over the 99 samples was taken and used along with the peak value of the multislit spectra to construct a S/N ratio. This S/N ratio is plotted in Figure 9 (c) and emulates the multislit instrument's performance based on detector noise only. It is worthwhile to note that the S/N curve constructed has a slope similar to the multislit S/N in the low source strength regions.

Figure 10 compares signal-to-noise ratios for the same slit widths in single slit and multislit configurations. Curve (a) is transferred from Figure 9 and is the multislit instruments signal to noise based on detector noise only. Curve (b) represents the calculated single slit performance by dividing curve (a) by  $N^{1/2}/2$ . Curve (c) shows the actual test data for a 50  $\mu\text{m}$  single slit configurations. There is fairly good agreement between the calculated and measured S/N ratios for the single slit configuration.

The S/N ratio improvement obtained can be better quantified by Figure 11. Here we ratio the multislit S/N to the single slit S/N for the low illumination levels where the multislit instrument seems to yield an improvement ( $L_{\text{source}} \leq 70 \mu\text{W}/\text{m}^2$ ). The comparison with the 50  $\mu\text{m}$  single slit yields an improvement of approximately 4.14, while the comparison with the 100  $\mu\text{m}$  single slit yields an improvement of 2.08, as opposed to the

theoretical factor of 7.92.

#### V. CONCLUSION AND COMMENTS

The constructed Hadamard transform spectrometer has displayed the capability of simultaneously capturing spatially encoded spectral information. The encoded spectrum of a Xe line source and a broader 13 nm interference filter source have been successfully reconstructed. Under conditions of low illumination levels the multislit instrument has displayed a S/N improvement of a factor of 2.08 over a single slit instrument with the same spectral resolution.

Our analysis of the data obtained suggests that the performance of the breadboard multislit instrument may be improved by enhancing the performance of the optical system. A more advanced optical design which would better image the extended entrance mask onto the focal plane would improve the multislit instrument's spectral resolution and limit encodegram error, increasing the system's upper S/N ratio limit. The multislit instrument was also examined with an  $N=503$ ,  $50 \mu\text{m}$  slit width entrance mask. The performance of the HTS in this configuration was very limited as the effects of optical aberration, anamorphic magnification, and second order diffraction combined to severely degrade the performance of the multislit instrument.

It should be noted here that an alternate technique was attempted to decode the spectral information from the spatially encoded data. The spectral data presented here were decoded by transformation of the spatially encoded voltage outputs by a binary S-matrix. The S-matrix consisted of ones and zeros exclusively, assuming perfect optical imaging, linear shift invariance, and uniform detector and grating efficiencies. We have attempted to replace the binary S-matrix with a weighted W-matrix which contains the actual weighting coefficients corresponding to our instrument's imaging and dispersion properties. The W-matrix was constructed by obtaining an encodegram at each of the instruments 251 spectral elements. These 251 data files were obtained by using a monochrometer with a Xe arc lamp as a calibrated source in an F/2 configuration. Application of this inverse W-matrix has resulted in successful reconstruction of any of the 251 data files obtained in this original data set, however, application of the W-matrix to any unknown, polychromatic source results in a spectra which contains no recognizable spectral information. We attribute this poor performance of the W-matrix transformation to the difference between the instrument constructed and instrument modeled in theory.

The theoretical application of the S-matrix to decode the spectra demanded a circulant matrix where each row could be obtained by any other row after a linear shifting of the

elements. The W-matrix obtained is comprised of individual encodegrams which vary in amplitude by as much as a factor of 3 due to differences in grating efficiency and detector responsivity. In addition, the spatial variation of each encodegram is different because of the non-uniform dispersion and blurring of each of the different slit positions. Furthermore, our film mask is neither perfectly opaque or perfectly transmitting, and random noise is also present from detector dark current variation and optical crosstalk. Simulation of an  $N=7$ , Hadamard encoded system has shown that as the W-matrix departs from the circulant properties present in the S-matrix the quality of the spectral reconstruction degrades. We believe that the variation of the different encodegrams used to make up this instrument's W-matrix is significant enough to make reconstruction of the spectral information impossible. Application of the W-matrix technique requires an instrument with similar spectral responsivities and a more uniform point spread function across the entrance mask.

## VI. ACKNOWLEDGEMENTS

The authors wish to acknowledge Tom Mikes and Charles Hatch of American Holographic, Littleton, Ma, for design of the grating and construction of the instrument, and also Stephen Davis of Real Time Engineering, Inc., Holliston, Ma, for software development. This work was supported by Phillips Laboratory under contract number F19628-85-C-0103.

## VII. REFERENCES

1. J. A. Decker Jr., "Experimental Realization of the Multiplex Advantage with a Hadamard Transform Spectrometer", *Appl. Opt.* **10**, 510-514, (1971).
2. M. J. E. Golay, "Multi-slit Spectrometry", *J. Opt. Soc. Am.* **39**, 437-444, (1949); "Static Multislit Spectrometry and its application to the Panoramic Display of Infrared Spectra", *J. Opt. Soc. Am.* **41**, 468-472, (1951).
3. N. J. A. Sloane, "Reducing the Number of Measurements in Doubly Multiplexed Spectrometers", in *Aspen Int. Conf. on Fourier Spectroscopy, 1970*, G. A. Vanasse, A. T. Stair, and D. J. Baker, Eds., (Air Force Cambridge Research Laboratories, 1971), pp. 435-440.
4. R. A. Van Tassel and W. K. Wong, "Hadamard-Coded, Stationary-Entrance-Mask, Photodiode-Array Spectrometer" in *7th International Conference on Fourier Transform Spectroscopy*, D. G. Cameron Ed., 1145, (1989), pp. 384-390.

5. J. L. Robichaud, W. K. Wong, and R. A. Van Tassel, "Measured Performance of a Hadamard-coded Photodiode-array Spectrometer", in *8th International Conference on Fourier Transform Spectroscopy*, H. M. Heise, E. H. Korte, and H. W. Siesler, Eds., 1575, (1992), pp. 255-257.
6. M. Harwit and N. J. A. Sloane, *Hadamard Transform Optics*, (Academic Press, New York, N. Y., 1979).
7. H. A. Rowland, "On Concave Gratings for Optical Purposeses", Amer. J. Sci. (3) 26, 87-98, (1883).

**Figure 1:** Comparison of conventional single slit, photodiode-array spectrometer and Hadamard transform spectrometer.

**Figure 2:** Photograph of Hadamard transform spectrometer.

**Figure 3:** Experimental layout of HTS with narrow-bandpass filtered source.

**Figure 4:** Xe pen lamp spectra obtained with 100  $\mu\text{m}$  single slit spectrometer.

**Figure 5:** Xe pen lamp spectra reconstructed from Hadamard transform spectrometer.

**Figure 6:** Typical detector output encodegrams for the narrow-bandpass filter source at two different source strengths. The mean value of each encodegram has been removed for display.

**Figure 7:** Reconstructed spectra obtained from the HTS with three different source strengths.

**Figure 8:** Single slit spectra obtained with the same three source strengths as in Figure 7.

**Figure 9:** Comparison of the S/N ratios obtained in multislit (a) and single slit (b) configurations as a function of source irradiance. A third S/N ratio is constructed from the multislit peak signal and a detector dark voltage term (c) as described in the text. This third S/N ratio (c) is used to simulate the performance of a HTS which is S/N limited by detector dark voltage temporal variation.

**Figure 10:** Comparison of the single slit S/N ratio obtained with a 50  $\mu\text{m}$  entrance slit (c) and the same S/N as calculated (b) from the detector dark voltage limited multislit S/N ratio (a).

**Figure 11:** S/N ratio improvement obtained with the HTS compared with the 50  $\mu\text{m}$  single slit spectrometer, the 100  $\mu\text{m}$  single slit spectrometer which has comparable resolution, and the theoretical limit of  $N^{1/2}/2$ .

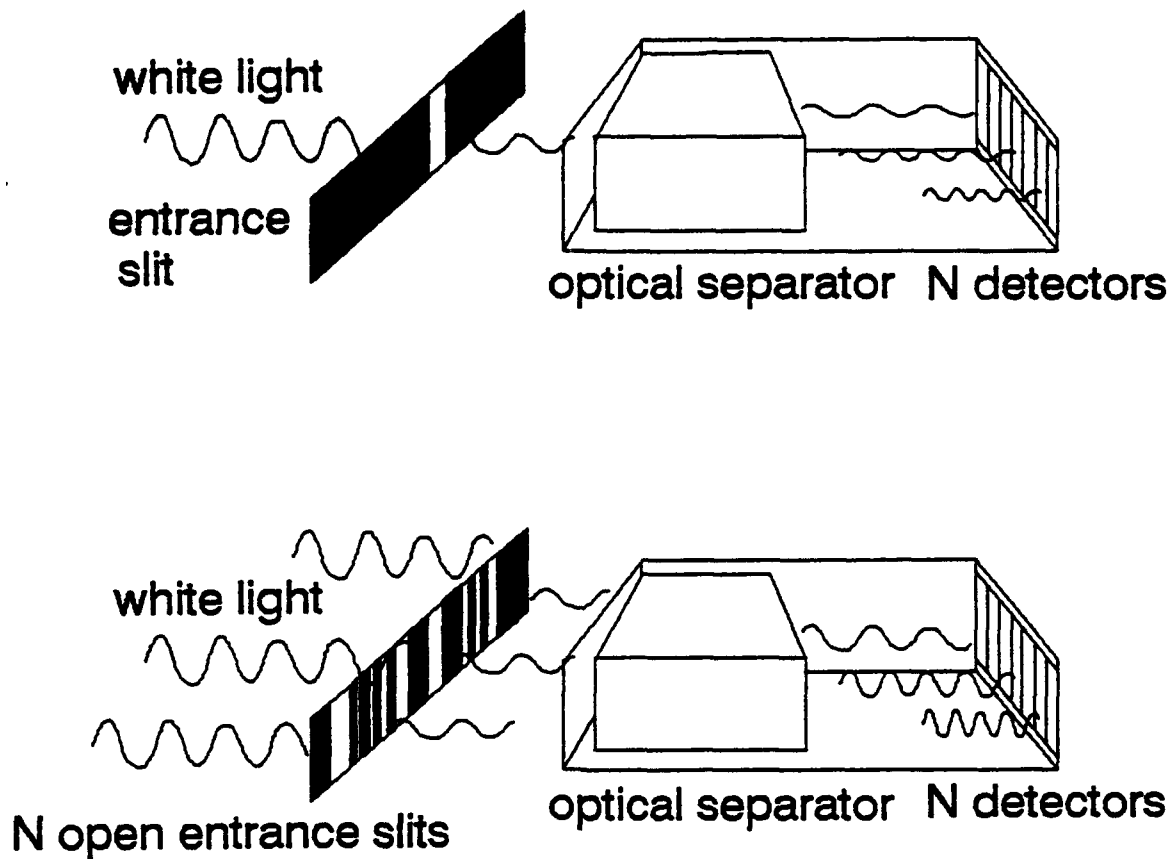


**Figure 1:** Comparison of conventional single slit, photodiode-array spectrometer and Hadamard transform spectrometer.

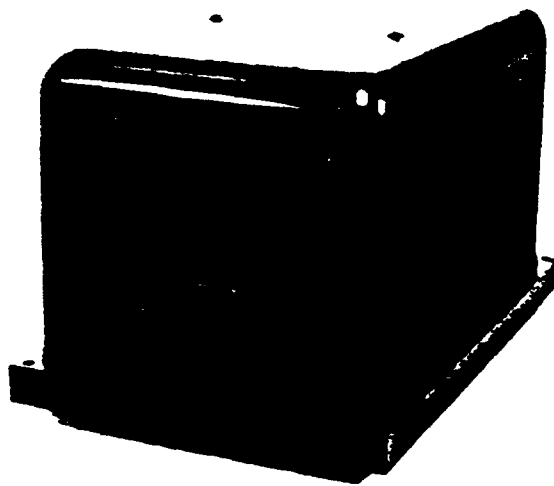


**Figure 2:** Photograph of Hadamard Transform Spectrometer

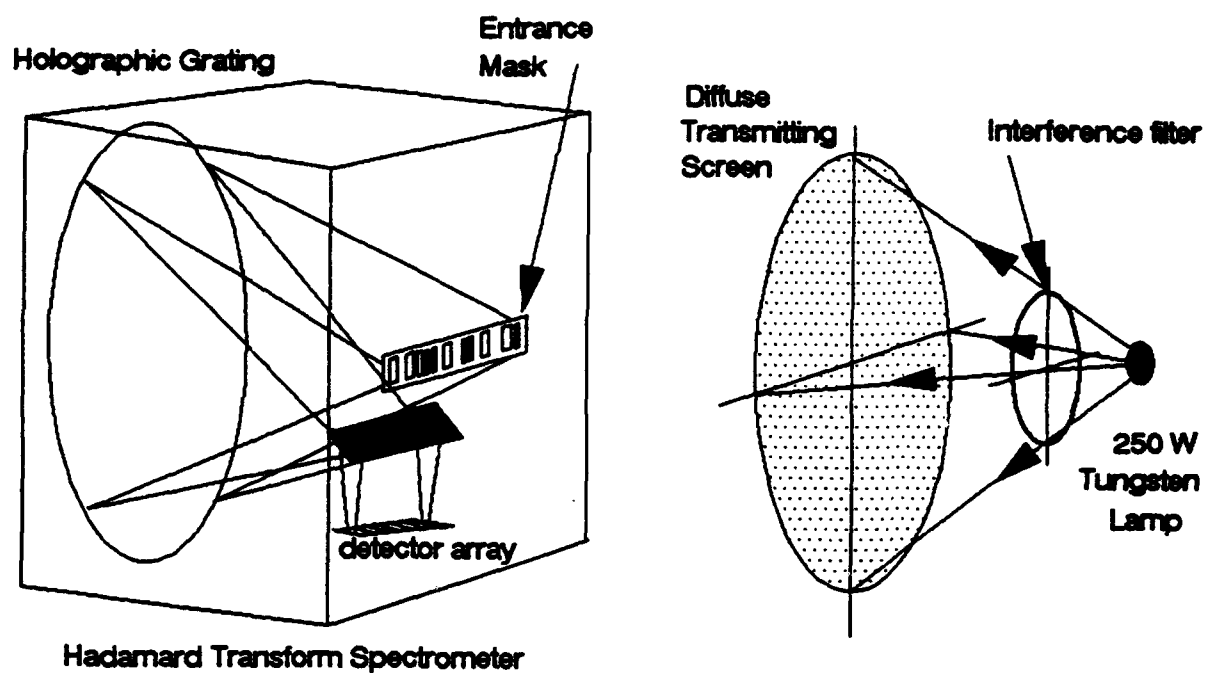


**Figure 3:** Experimental layout of HTS with narrow-bandpass filtered source.

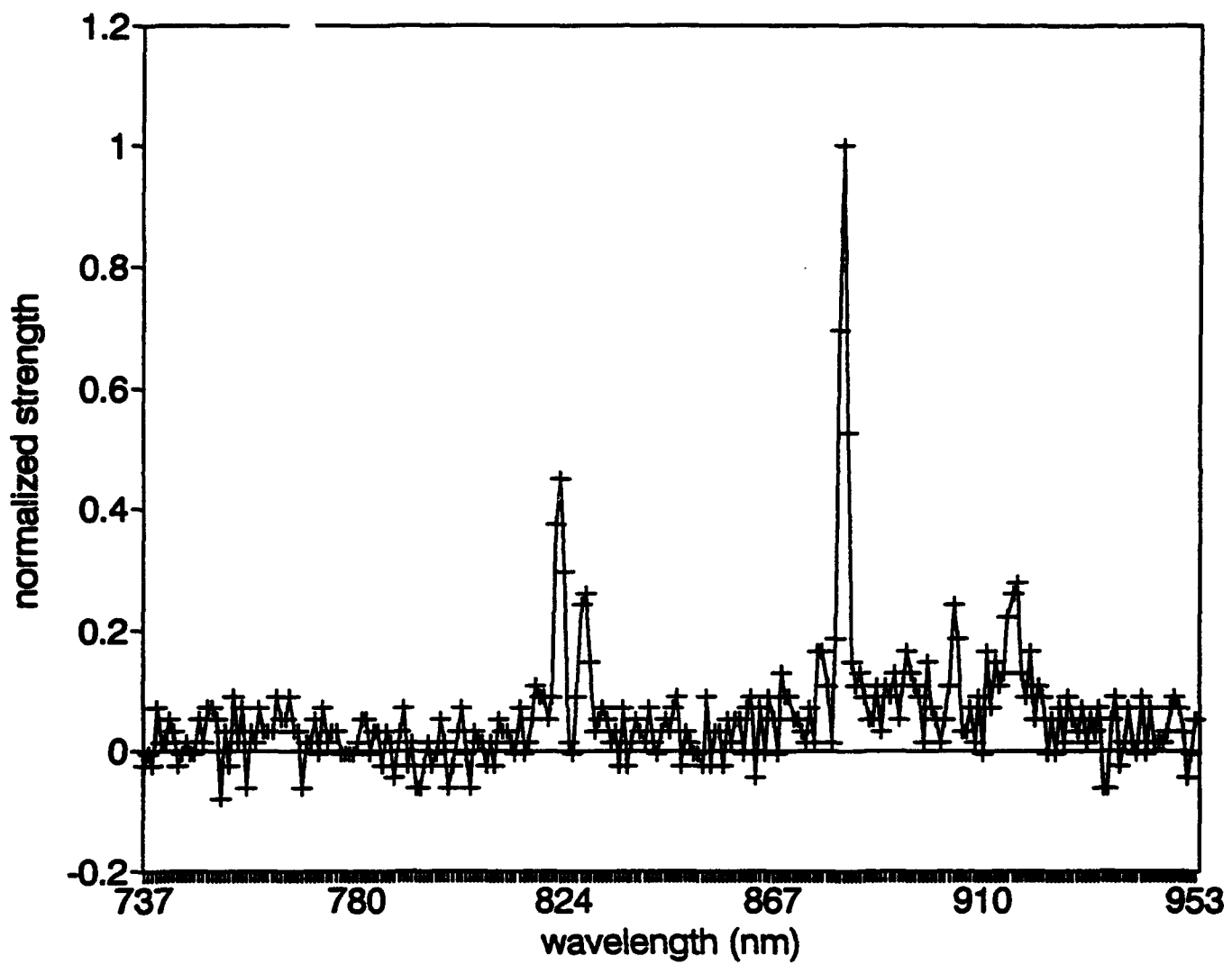


**Figure 4:** Xe pen lamp spectra obtained with 100  $\mu\text{m}$  single slit spectrometer.

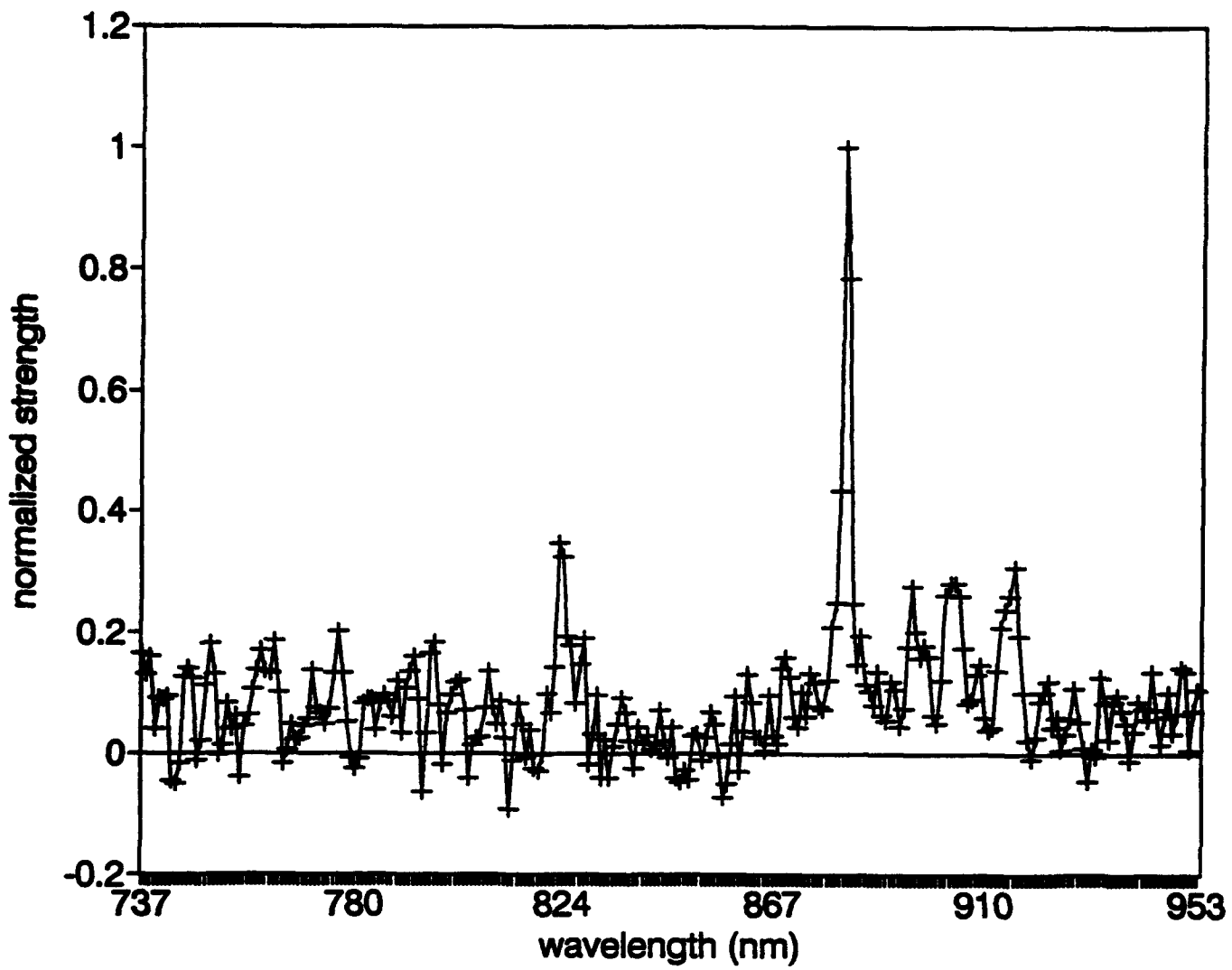


**Figure 5:** Xe pen lamp spectra reconstructed from Hadamard transform spectrometer.

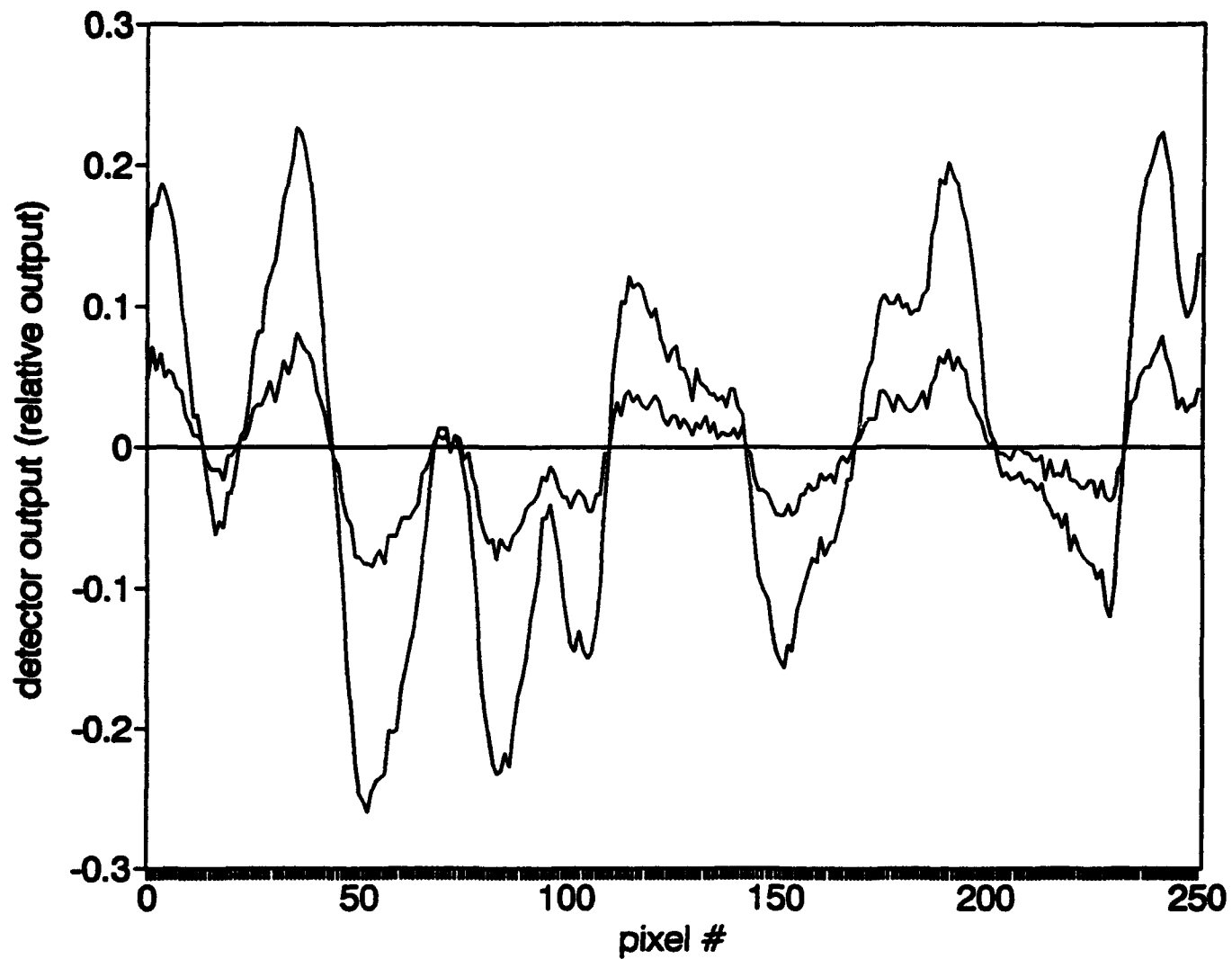


**Figure 6:** Typical detector output encodegrams for the narrow-bandpass filter source at two different source strengths. The mean value of each encodegram has been removed for display.

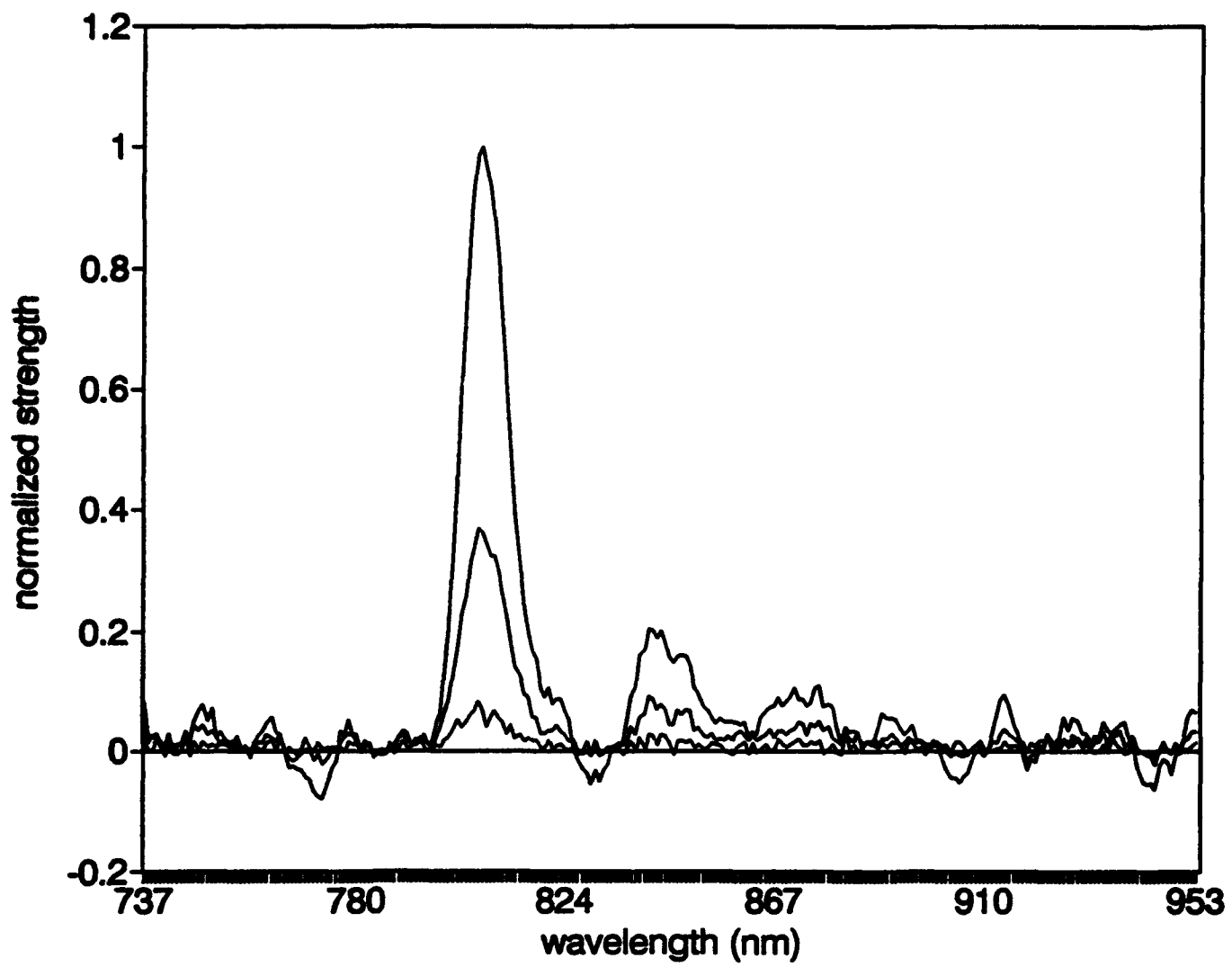


**Figure 7:** Reconstructed spectra obtained from the HTS with three different source strengths.

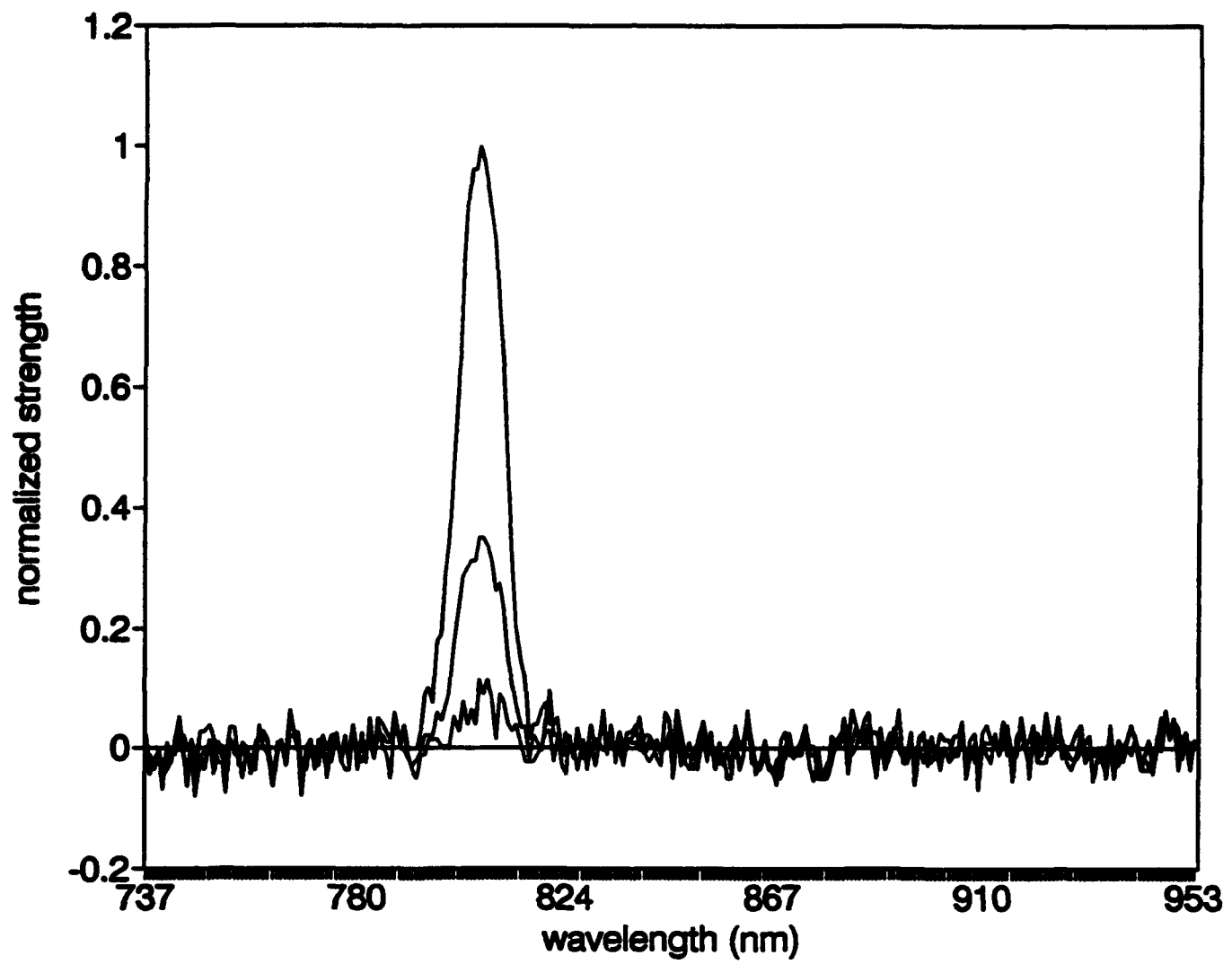


**Figure 8:** Single slit spectra obtained with the same three source strengths as in Figure 7.

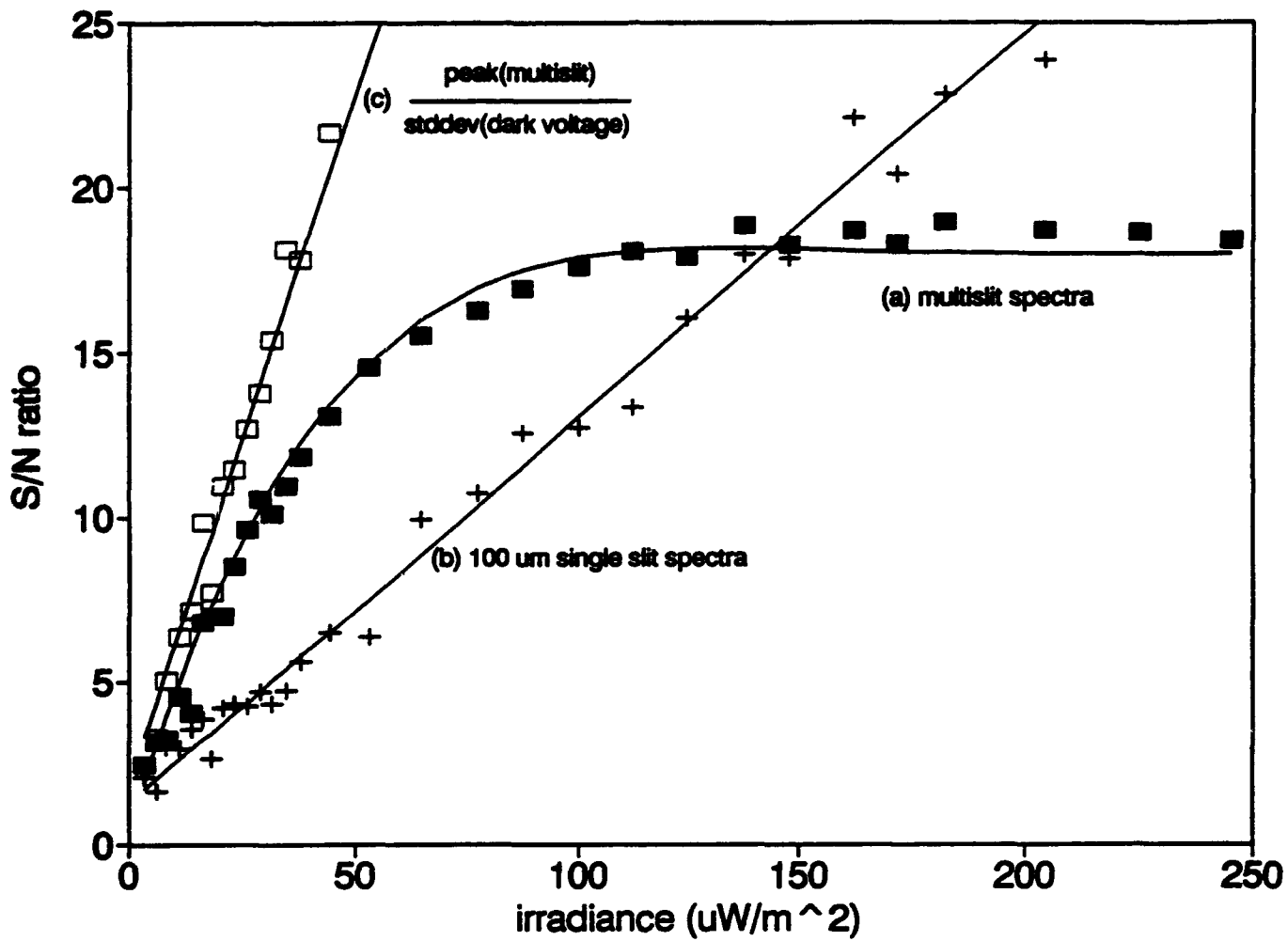
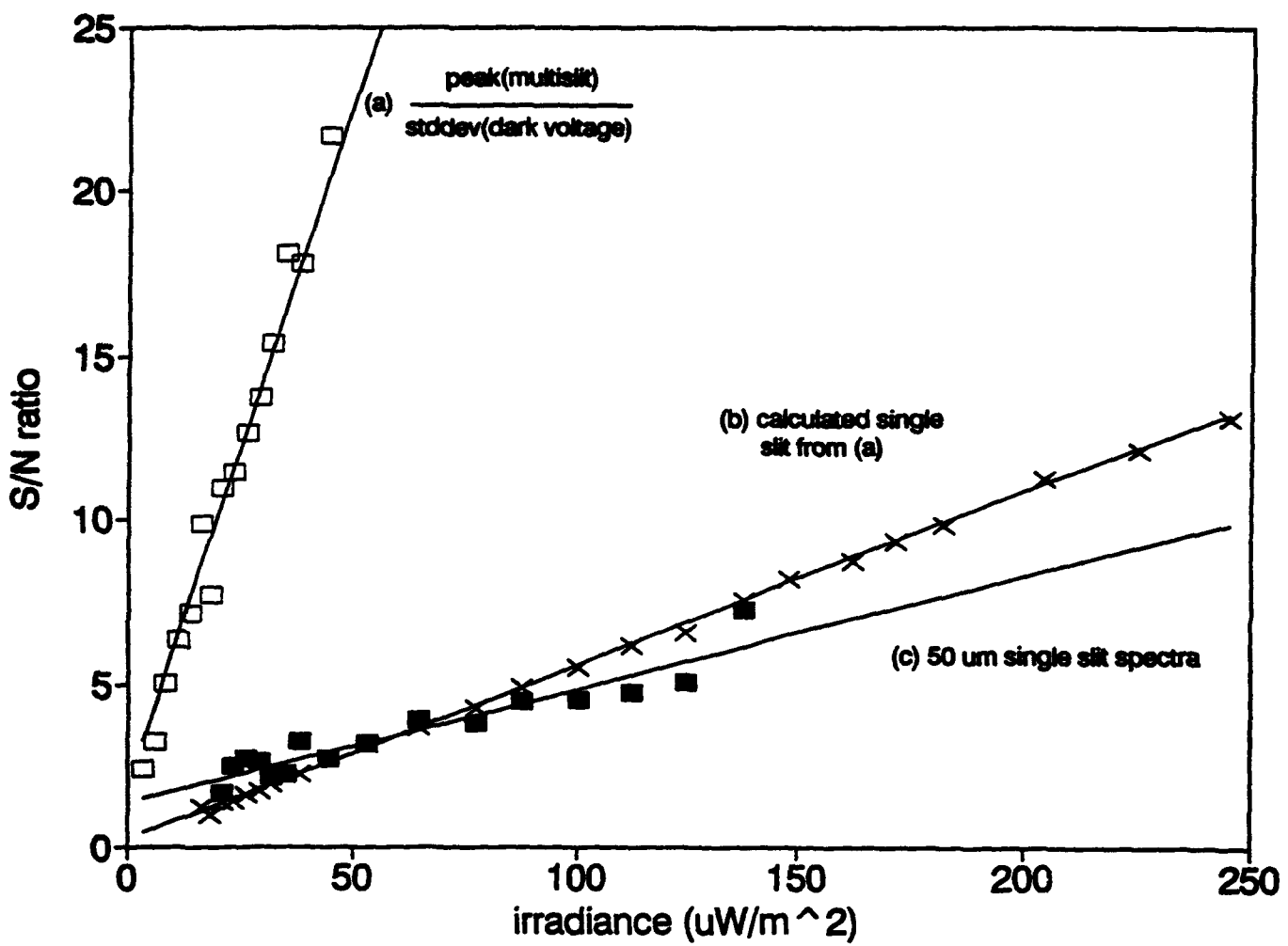
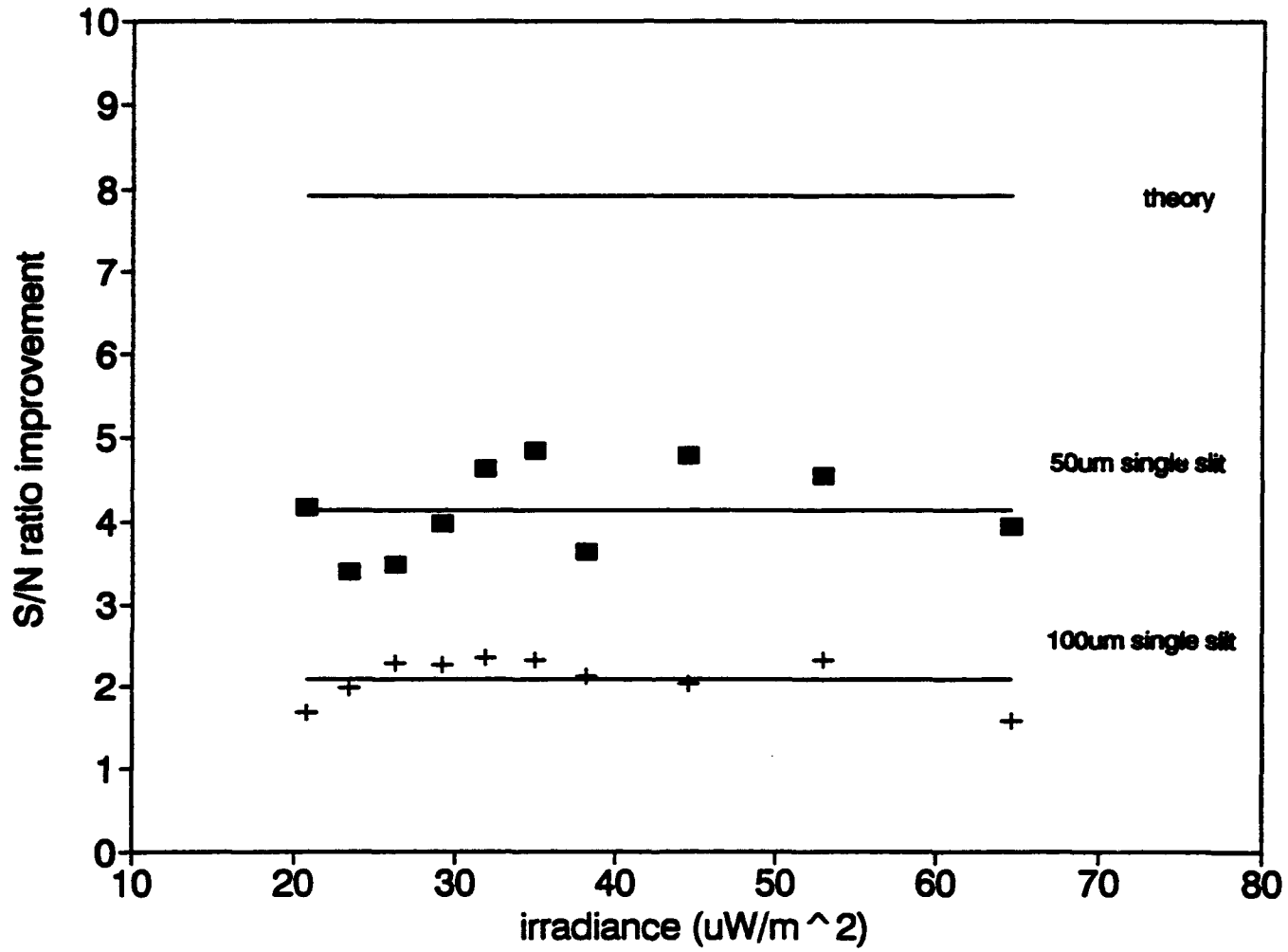


Figure 9: Comparison of the S/N ratios obtained in multislit (a) and single slit (b) configurations as a function of source irradiance. A third S/N ratio is constructed from the multislit peak signal and a detector dark voltage term (c) as described in the text. This third S/N ratio (c) is used to simulate the performance of a HTS which is S/N limited by detector dark voltage temporal variation.



**Figure 10:** Comparison of the single slit S/N ratio obtained with a 50  $\mu\text{m}$  entrance slit (c) and the same S/N as calculated (b) from the detector dark voltage limited multislit S/N ratio (a).



**Figure 11:** S/N ratio improvement obtained with the HTS compared with the 50  $\mu\text{m}$  single slit spectrometer, the 100  $\mu\text{m}$  single slit spectrometer which has comparable resolution, and the theoretical limit of  $N^{1/2}/2$ .

**Part 2.**

**Topic 2. Contamination Degradation Program**

**Principal Investigator: Mr. James J. Guregian**

## CONTAMINATION DEGRADATION PROGRAM

### OBJECTIVE:

To measure the BRDF of the primary mirror in the CIRRIS chamber externally. To monitor the BRDF through a series of warm to cold cycles, and to analyze the effect of contamination degradation on the scatter characteristics of the test mirror.

### PROCEDURE:

1. First baseline BRDF bench measurements of the CIRRIS primary mirror were performed with SSG's standard BRDF test station. Two spots were measured on the mirror. The BRDF measured a moderate to low number of  $7.0 \text{ e-}4 @ 1^\circ$  (Figure 1). A non superfinished CIRRIS primary was tested as well to verify the apparatus, it had a BRDF of  $5.0 \text{ e-}1 @ 1^\circ$ .
2. The next step was to install the test mirror in the telescope, mount it in the CIRRIS chamber, and repeat the measurements with the external BRDF station (Figure 2).

The first tests were done with the chamber open. After slight modifications of the light trap, the measurements from the external BRDF station were consistent with the BRDF calculated from the bench test.

The CIRRIS chamber was then closed. The measurements were again similar to the baseline, therefore the external BRDF station provided to be operational.

3. We were now able to run the chamber through a series of cryo cycles monitoring the primary mirrors BRDF at each step. We proceeded as follows:
  - a. BRDF with the chamber closed, no vacuum
  - b. BRDF with the chamber under vacuum, roughing pump 20 hours
  - c. BRDF after running turbomolecular pump 8 hours (Figure 3)
  - d. Cooled chamber down to 100K (Figure 4)
  - e. Warmed the system back to room temperature
  - f. Vented the system back to atmospheric pressure
  - g. Repeated steps a through f (Figure 5)
4. Finally, the CIRRIS primary was removed from the chamber and returned to the test bench. BRDF measurements were again recorded to verify the mirrors status.

## RESULTS AND CONCLUSIONS

The CIRRIS primary consistently measured a BRDF of 7 e-4 at 1 degree. Results from the bench test, and the external BRDF measurements were in complete correlation. Fluctuations in the external BRDF data, were well within experimental error. Two complete warm to cold cycles were performed on the primary, with no measurable change in the BRDF. Figure 6 is a composite graph of the BRDF measurements from the test bench. CIRRIS chamber, first cold cycle, second cold cycle, and the final ambient state of the CIRRIS primary mirror.

Currently the CIRRIS primary is undergoing the process of being re-superfinished. The mirror tested to be an average low scatter optic. We would like to repeat this test with a mirror of BRDF of 1 e-4 at 1°. A higher quality mirror will increase our sensitivity in monitoring the contamination during our tests.

DATA: External BRDF of CIRRIS primary through 2 cryo cycles.

Date/Time	3°	5.5°	7.7°	Comments
2/2/88	.			no vacuum
1430	34 mV	18 mV	10 mV	begin pumping 1435
1700	36 mV	18.4 mV	10 mV	300 mtorr
2/3/88				75 mtorr
0900	40 mV	21.2 mV	11 mV	turbo on
1100	38 mV	18.6 mV	11 mV	35 mtorr
1300	42 mV	19 mV	10.8 mV	1600 n2 flowing
2/4/88				15 mtorr
0900	52 mV	18.4 mV	9 mV	180K
2/5/88				15 mtorr
1000	52 mV	21 mV	11.4 mV	300K
1315	46 mV	21 mV	10.4 mV	P atm
1530	36 mV	18 mV	10 mV	50 mtorr
2/7/88				25 mtorr
1630	52 mV	19.4 mV	10.6 mV	300K, n2 flowing
2/8/88				15 mtorr
0900	34.2 mV	17.4 mV	10 mV	160K
1600	36 mV	18 mV	9.6 mV	100K
2/10/88				290K
0930	38 mV	16.0 mV	10 mV	
1000	38 mV	16.8 mV	10 mV	P atm

Laser power 8 W chopped to 4 W

Date:

Date: Jan. 25, 1988

NERC Detector  
Black-Body Calibration

BRDF Bench Test of CIRRIS Primary

Spot A (Clean)

6.70E+04 V/W

POW (DET.) 5.50 (wATTS)  
 LAMBDAA 10.6 (microns)  
 IFOV 4.30E-05 (sr)  
 SPEC ANG 30.00 (deg)  
 CW POW 18.00 (watts)  
 CHOP FRE 4.00 (hz)  
 INC ANG 5.00 (deg)

FILTER TABLE  
 ABEF 1.00E-08  
 AF —  
 BE —

IRIS APERTURE =  
 NONE (INCHES)

BENCH ANG	SIGNAL (mV)	FILT. VAL.	Vs/Vso	O.F.A.	B-B0	BRDF (B-B0)	LOG B-B0	LOG BRDF	1/THETA SQ	LOG (THEGA <sup>-1</sup> )
30.00	6.00	1.00E-08	3.69E+08	0.00	0.00000	2.326E+04	-1.78021334		4.000E-04	-3.3979
32.00	2.700	1.00E+00	7.33E-09	2.00	0.03471	1.705E-04	-1.45959136	-3.76827	1.000E-04	-4.0000
33.00	1.750	1.00E+00	4.75E-09	3.00	0.05201	1.108E-04	-1.28393258	-3.95627	4.444E-05	-4.3522
34.00	1.380	1.00E+00	3.69E-09	4.00	0.06827	8.804E-05	-1.19948080	-4.06530	2.500E-05	-4.6021
35.00	1.250	1.00E+00	3.39E-09	5.00	0.08648	7.919E-05	-1.08310234	-4.10134	1.800E-05	-4.7959
36.00	1.030	1.00E+00	2.80E-09	6.00	0.10363	6.536E-05	-0.98449731	-4.18468	1.111E-05	-4.9542
37.00	1.000	1.00E+00	2.71E-09	7.00	0.12073	6.358E-05	-0.91817148	-4.19665	8.163E-06	-5.0881
38.00	0.820	1.00E+00	2.23E-09	8.00	0.13777	5.226E-05	-0.88084532	-4.28184	6.250E-06	-5.2041
39.00	0.680	1.00E+00	1.85E-09	9.00	0.15474	4.345E-05	-0.81040350	-4.36201	4.938E-06	-5.3084
40.00	0.660	1.00E+00	1.87E-09	10.00	0.17163	4.422E-05	-0.78540174	-4.35441	4.000E-06	-5.3979
42.00	0.500	1.00E+00	1.38E-09	12.00	0.20518	3.226E-05	-0.68786744	-4.49134	2.778E-06	-5.5563
44.00	0.400	1.00E+00	1.08E-09	14.00	0.23837	2.802E-05	-0.62274902	-4.58475	2.041E-06	-5.8902
46.00	0.260	1.00E+00	7.06E-10	16.00	0.27116	1.707E-05	-0.56676787	-4.76778	1.563E-06	-5.8062
48.00	0.146	1.00E+00	3.98E-10	18.00	0.30352	9.888E-06	-0.51780971	-5.01378	1.235E-06	-5.9085
50.00	0.130	1.00E+00	3.53E-10	20.00	0.33540	8.731E-06	-0.47443135	-5.05895	1.000E-06	-6.0000

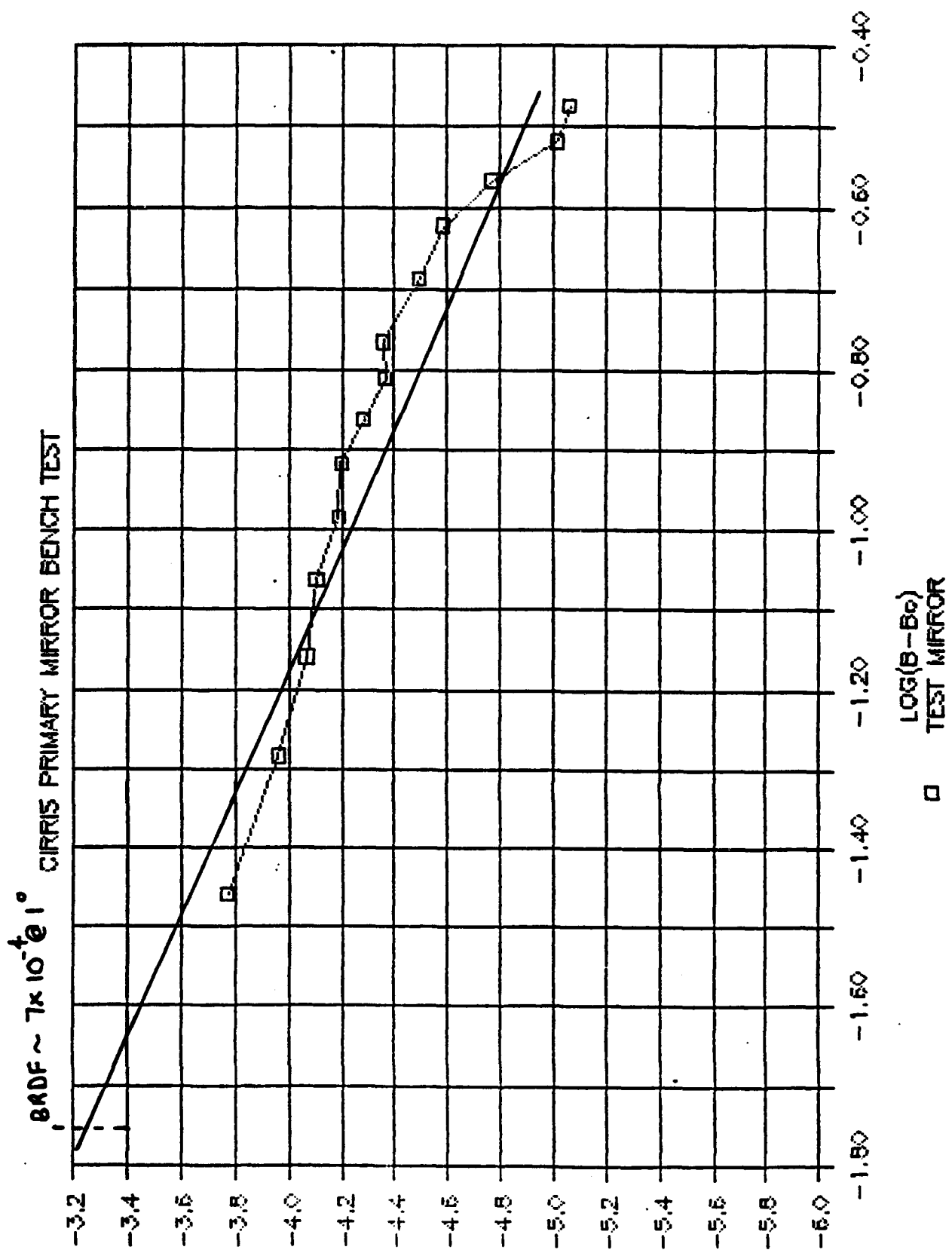


Figure 1

## EXTERNAL BRDF MEASUREMENT

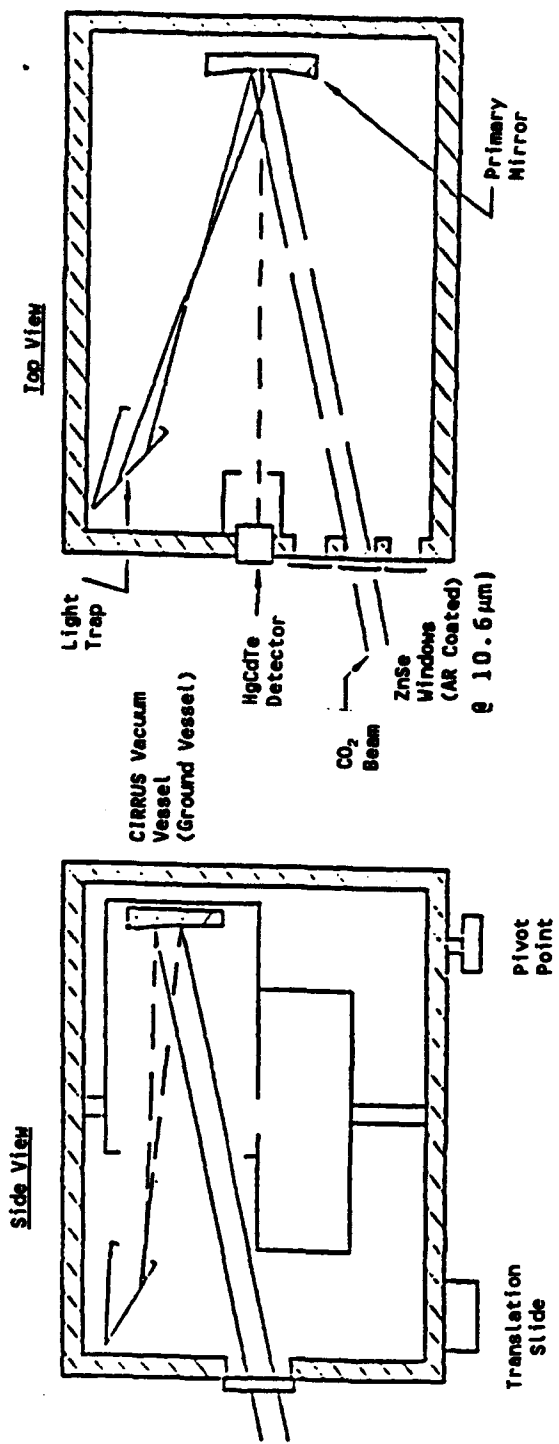


Figure 2

CIRCUIT PRIMARY ERDF UNDER VACUUM

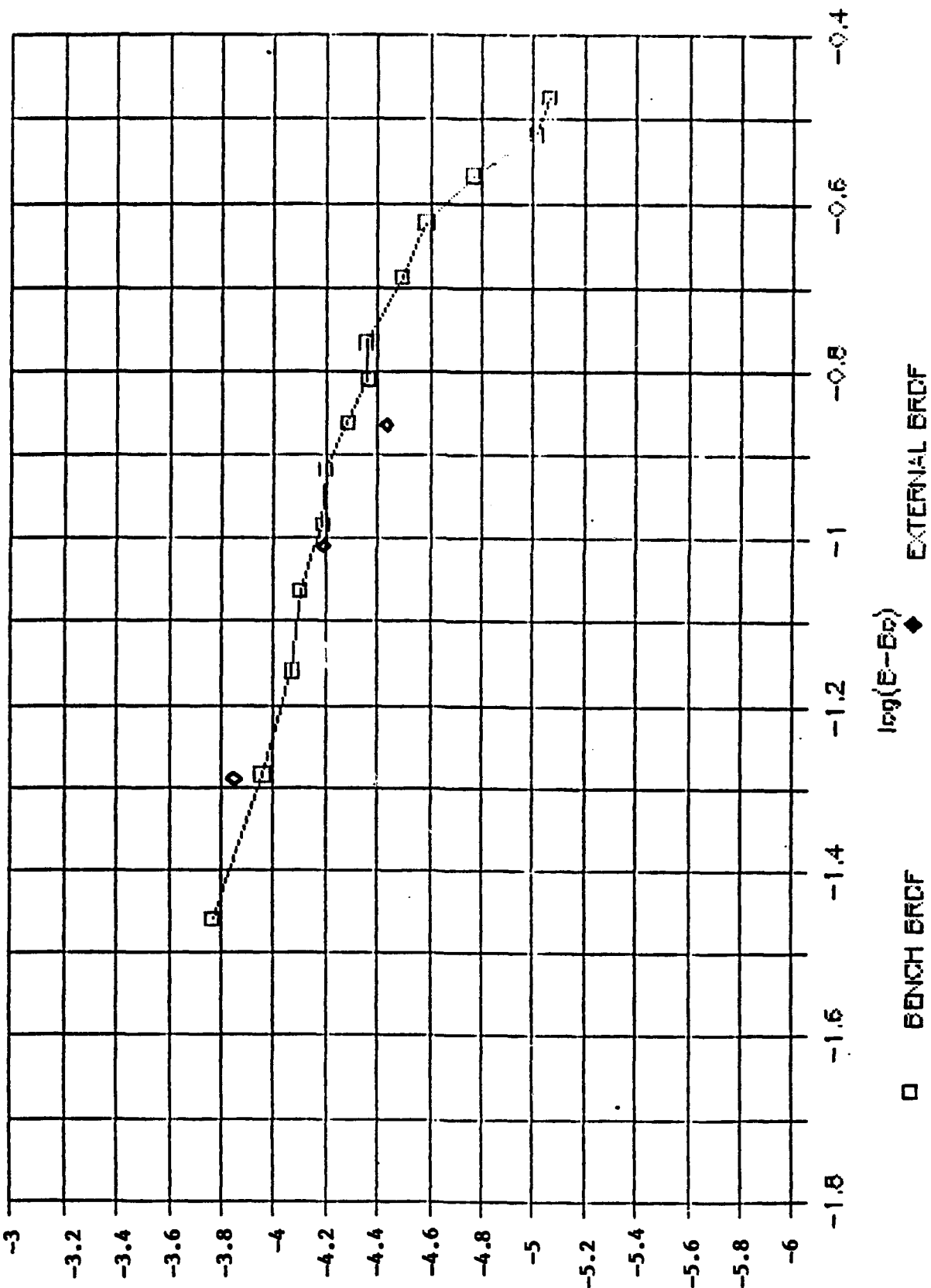


Figure 3

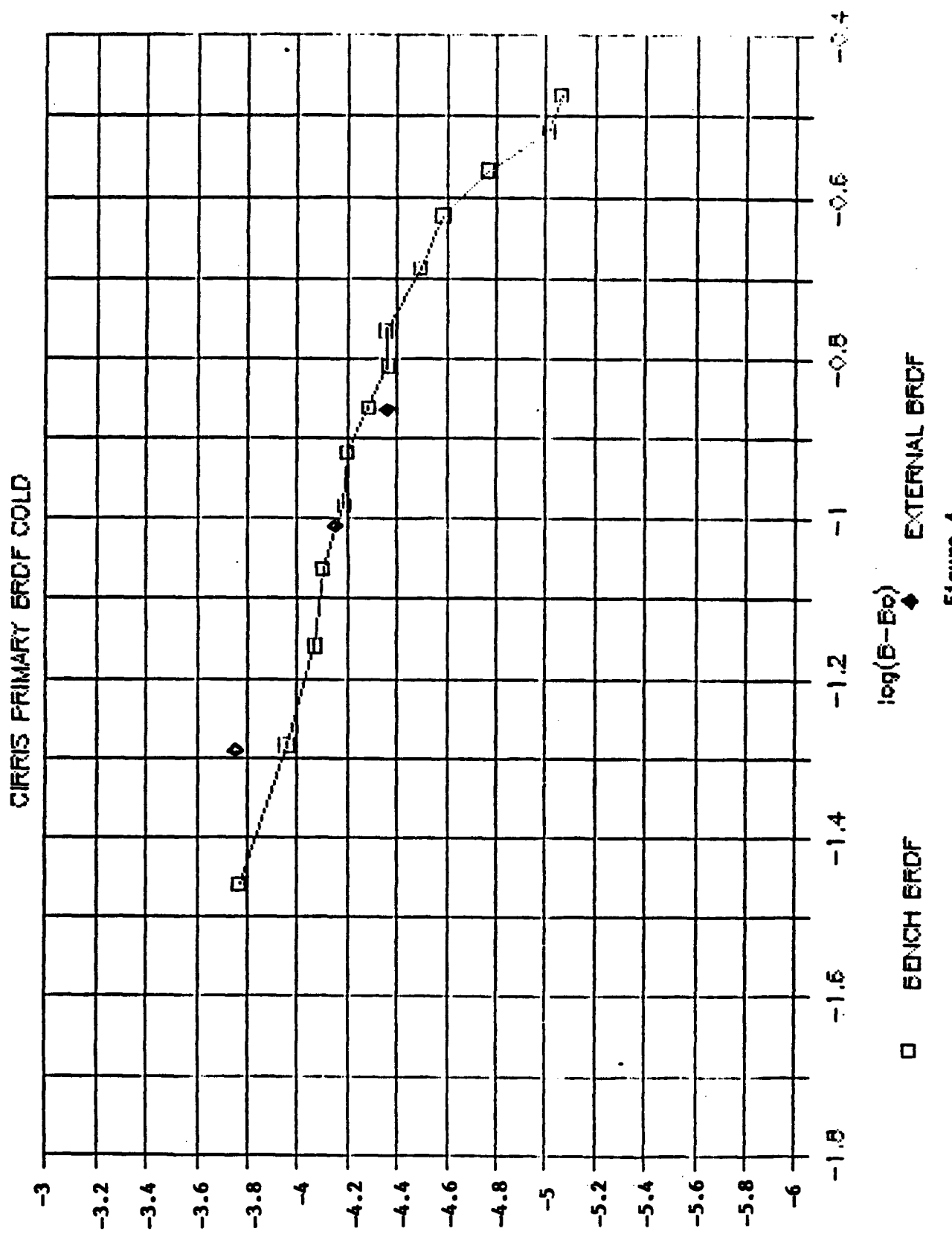


Figure 4

CIRRIS PRIMARY BRDF AFTER 2 CYCLES

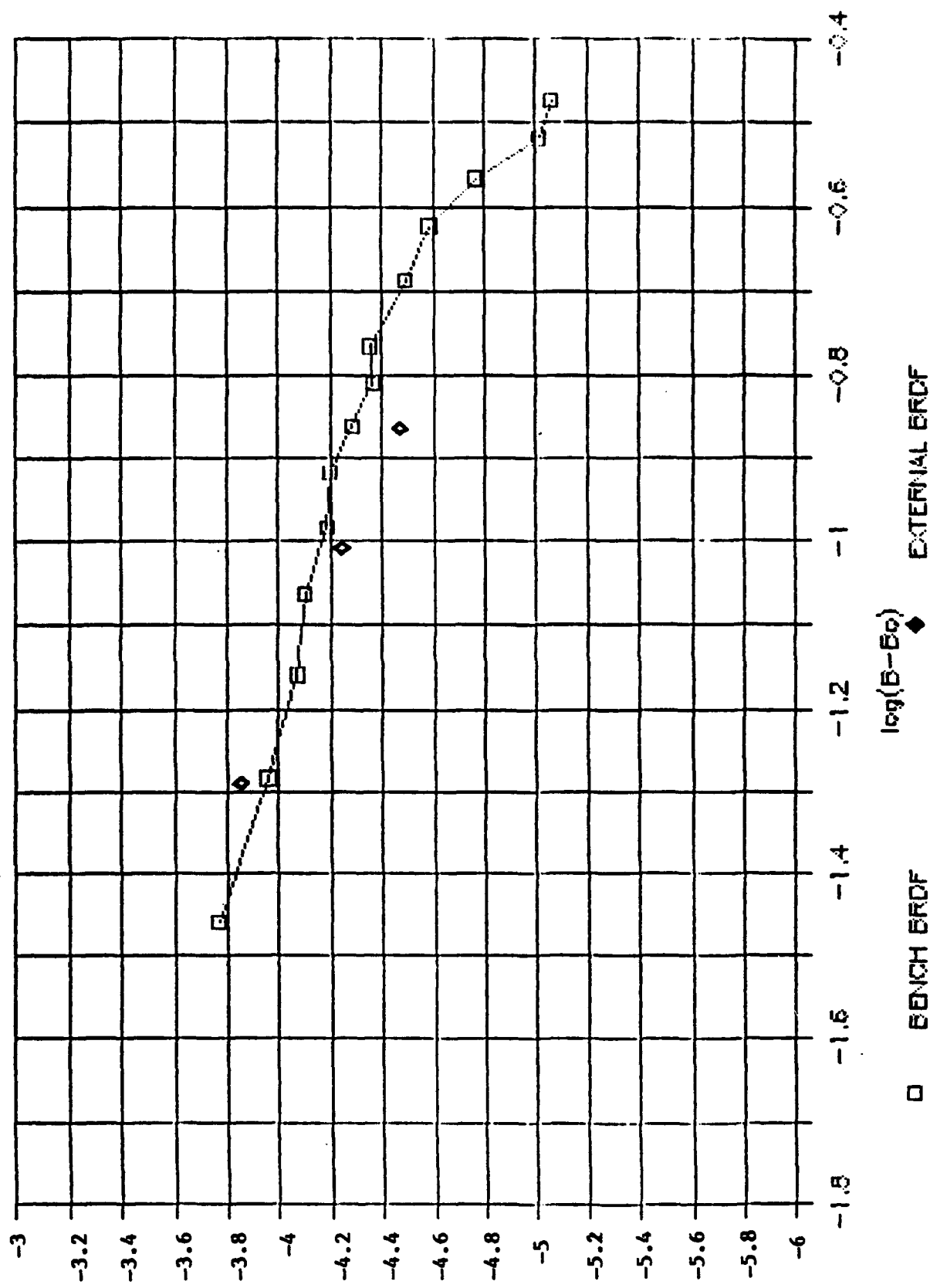


Figure 5

CIRRUS PRIMARY BRDF COMPOSITE

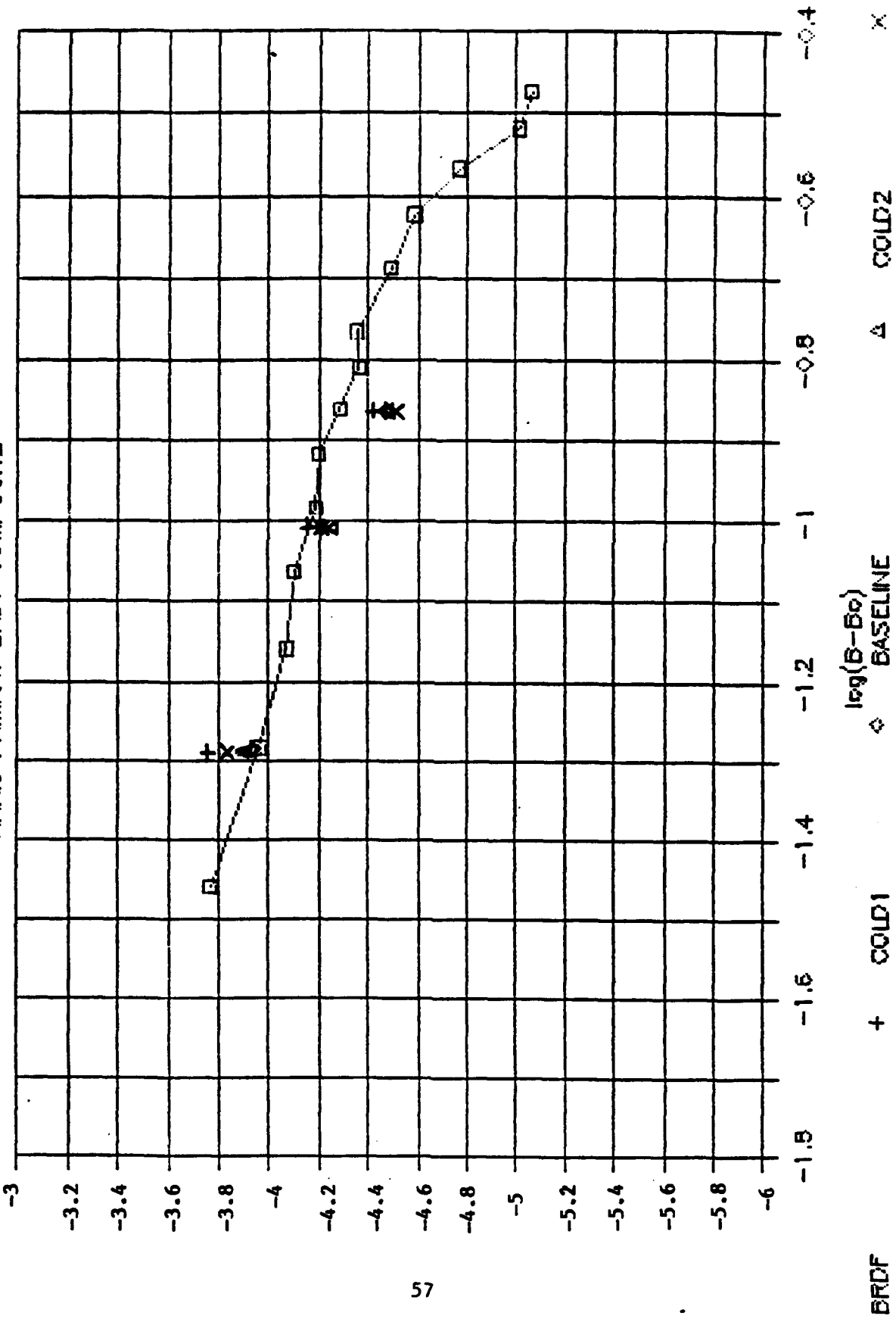


Figure 6

**Part 3.**

**Topic 3. Supersensitive IR Spectrometer for Spatial Measurements**

**Principal Investigator: Dr. Holger M. Luther**

## PHASE 1 - DESIGN

The design study conducted during the first phase of this effort identified a number of spectral measurement programs that will derive a substantial benefit from the utilization of a cryogenic infrared spectrometer composed of a Fabry-Perot Interferometer and the Rockwell Solid State Photomultiplier (SSPM). The combination of the extremely narrow spectral bandpass and the very low noise equivalent power (NEP) of the SSPM would make possible the ground-based observation of auroral phenomena in certain spectral window regions of the atmosphere and upper atmospheric emission phenomena generally. Satellite or rocket-borne remote sensors equipped with the above spectrometer could be used to investigate earth limb radiance mechanisms at tangent heights as low as 80 km and to conduct boost phase surveillance missions.

It was the intention of the second phase of this program to obtain a cryogenic Fabry-Perot interferometer from NRL, an SSPM from Rockwell International and to install that combination in the LABCEDE or COCHISE chambers of the AF Geophysics Laboratory to verify the performance predictions derived in the study phase of the program. This effort, however, was redirected when it became apparent that the NRL interferometer would not be available to the program. The redirected program effort consisted of a design analysis of a user-friendly, transportable, cryogenic Fabry-Perot interferometer based on the technical approach adopted by NRL. The statement of work included the following tasks:

1. Formulate an instrument concept that utilizes the technical approach of the NRL interferometer.
2. Identify its critical components and determine if these can be fabricated to the required specifications using presently available technologies.
3. Design and detail the spectrometer components and place orders for those that require long procurement times.
4. Estimate the performance of the instrument and present the results of the design analysis in a design review.

These tasks were completed on or before 15 August 1988, and a preliminary design review was held on 31 August 1989.

## 2.0 TECHNICAL APPROACH

Infrared Fabry-Perot interferometers using planar and spherical cavity mirrors

are available commercially from various vendors such as Burleigh Instrument Corp. These instruments are generally constructed from materials that have very low thermal expansion coefficients, such as Invar or Super Invar. The control of the cavity mirror spacing is accomplished with the aid of piezoelectric drivers and high precision mechanical lead screws. The interferometers therefore rely on highly stable mechanical mirror support structures and piezoelectric actuators to set and maintain cavity spacing. This is proven technology for ambient temperature spectral measurement instrumentation which, however, cannot be utilized at cryogenic temperatures since mechanical stability of the mirror mounts can no longer be maintained, the piezoelectric actuators are substantially impaired by the low temperature, and access to mechanical alignment micrometer screws is precluded by the dewar wall. Thus, the alignment and control of the cavity must be accomplished using electromechanical devices that can be used at cryogenic temperatures, while the mirror spacing is monitored with sensors that likewise are unaffected by the cold temperature or can be remotely connected to the etalon with the aid of fiberoptic cables. This is the approach adopted by Howard Smith (1) in the design of the NRL interferometer. Smith used voice coil drivers to move and control the mirror cavity spacing and three visible light etalons located at 120° intervals near the periphery of the IR etalon. These peripheral etalons sense the mirror cavity spacing and provide the error signal to the servo system which controls the power to the actuators.

This control concept was first developed by J. V. Ramsey (2) who noted that the cavity spacing of one etalon can be set at exactly that of another by illuminating the first (fixed) etalon with a broad band light and tuning the second one until the transmitted light reaches a maximum. The principle is illustrated in Figure 1 and is expressed mathematically as follows:

$$I(S, x) = \int_{\Delta\lambda} B(\lambda) (T_1^2 / (1 + (A_1 \sin \pi S/\lambda)^2)) (T_2^2 / (1 + (A_2 \sin \pi (S+x)/\lambda)^2)) d\lambda$$

where  $T$  is the transmittance of the etalons,  $B$  is the spectral distribution of the broad band light,  $S$  is the cavity spacing of the first etalon, and  $S+x$  is that of the second. The amplitude  $A$  of the Airy functions is given by  $A = 2F/\pi$  in which  $F$  is the effective finesse of the etalon. A numerical integration of the above intensity function reveals that  $I$  has maxima whenever  $x$  is a multiple of  $\lambda_c/2$  wherein  $\lambda_c$  is the wavelength at the peak of the spectral distribution of the incident light. The maxima, however, have a global peak when  $x = 0$ . This is seen in Figure 2 which shows the intensity of the transmitted light at discrete points in arbitrary units. The parameters  $S$  and  $\lambda_c$  have been chosen to be consistent with the expected cavity spacing of the actual IR etalon being designed and the center wavelength and width of the light from a Hitachi GaAlAs light emitting diode.

Smith utilized the above concept and refined it by splitting the light transmitted through the fixed (reference) etalon into two separate light paths which illuminated two control etalons at each of the three peripheral locations of the IR etalon. The etalon

cavity spacing of each such pair, moreover, differed by  $\lambda/4$  which caused the transmitted intensities to be 90° out of phase with each other. Thus a very tight control of the mirror cavity was achieved by nulling the difference signal obtained from each pair of control etalons.

The SSG control concept also utilizes Ramsey's principle, but instead of integrating the control etalons into the servo system, these will only be used to calibrate three differential eddy current sensors collocated with the control etalons. This concept is illustrated in the block diagram shown in Figure 3. The eddy current sensors used in the SSG interferometer are the KD-5100 series differential position sensors manufactured by the Kaman Instrumentation Company. These have been specifically designed to function at cryogenic temperatures and feature a noise equivalent displacement of  $10^{-7}$  mm/Hz<sup>1/2</sup>. Thus the residual displacement uncertainty for a 100 Hz servo system is on the order of 20 nm. This uncertainty is less than 1/200th of a wavelength in the MWIR.

### Etalon Finesse and Resolution

Jacquinot (3) has shown that the effective finesse  $F$  of a Fabry-Perot interferometer is generally limited by the surface roughness of the cavity mirrors and the residual tilt between them. Both tilt and surface may be given a component finesse analogous with the reflective finesse obtained from the first order theory of the F-P interferometer. The effective finesse is then obtained from sum of the squares of their reciprocals - e.g.,

$$1/F^2 = 1/F_p^2 + 1/F_r^2 + 1/F_t^2$$

wherein  $F_p$  is the parallelism finesse,  $F_r$  is the flatness finesse, and  $F_t$  is the reflective finesse. These may be computed from the following expressions:

$$F_p = m/3^{1/2} \text{ when mirrors are parallel to } \lambda/m$$

$$F_r = m/2 \text{ when mirror surface is flat to } \lambda/m$$

$$F_t = \pi R^{1/2}/(1-R) \text{ when } R \text{ is the mirror reflectance}$$

The resolution (full peak width at half maximum) is then given by the free spectral range divided by the effective finesse - i.e.,

$$\text{res.} = 1/(2SF) \text{ wave numbers}$$

The above expressions for the component finesses make it clear why the effective finesse is limited by the mirror surface conditions and the attainable parallelism of the cavity mirrors. IR transmissive materials are generally softer than those that are used

in the visible spectrum. Thus a substrate of ZnS or ZnSe polished to  $\lambda_{\text{noise}}/20$  is quite representative of today's state of technology. The above flatness then at a wavelength of 5  $\mu\text{m}$  yields an  $F$ , on the order of 80, while the noise equivalent displacement uncertainty of the Kaman displacement sensors lead to an  $F$ , that is on the order of 60, since one will have to double the aforementioned noise equivalent displacement to estimate the total tilt over the mirror aperture. The reflective finesse was therefore specified such that the effective finesse would be on the order of 50. Thus a free spectral range of 25  $\text{cm}^{-1}$  yields a resolution of 0.5  $\text{cm}^{-1}$  which is consistent with the requirements of the demonstration interferometer while the free spectral range is within range of the spectral bandpass of dielectric interference filters which must serve as order sorting filters.

### Interferometer Throughput

An ideal F-P interferometer illuminated with collimated, monochromatic light transmits a fraction of that light given by

$$T = (1 - A/(1-R))^2$$

wherein  $A$  is the absorption of the light within the mirror coating. This can be high when metallic coatings are used; but is on the order of 0.5 to 1.0% when dielectric mirrors are used. Thus, a reflectance of 95% and the above absorbtance yields a transmittance on the order of 64%. Hernandez (4) has shown, however, that the transmittance must be modified to include losses due to mirror imperfections and tilt. Thus, the transmittance becomes

$$T = T_{\text{ideal}} ((1-R)/(1-R_E))^2$$

wherein  $R_E$  is an effective reflectance determined from

$$R_E = 1 - \pi/F + (\pi/2F)^2$$

The above effective transmittance for  $F = 50$  is thus equal to 42%.

If the incident light is not collimated, the off-axis rays are attenuated due to the fact that the cavity spacing is diminished by the cosine of the angle of incidence. Thus Jacquinot (3) has shown that the solid angle subtense of an F-P interferometer of resolving power  $R$  ( $\lambda/\Delta\lambda$ ) is given by

$$d\theta = 2 \pi a/R$$

wherein  $a$  is an empirical factor on the order of 0.8. The above at a wavenumber of 2000  $\text{cm}^{-1}$  yields a half angle on the order of 0.00123 radians.

A figure of merit often used to compare the performance of spectrometers is the "etendu" which is the product of the aperture and  $d\Omega$ . Thus for the F-P interferometer one finds

$$E = A_{ap} 2\pi a/R$$

wherein  $A_{ap}$  is the aperture area of the cavity mirrors. This etendu is essentially identical to that of the Fourier-Michelson interferometer.

### Mechanical Construction

Figure 4 shows the layout of the interferometer. There are essentially three independently controlled actuators on the periphery of the suspended mirror mount. Each of these consists of two BEI/Kimco linear actuators (voice coil motors) so located that their center of effort coincides with the location of the Kaman position sensor which controls these VCM's. The VCM's have a combined motor constant of 1 lb/A to allow the interferometer to function in any orientation, since the suspended mirror frame weighs about 2 lbs. and the maximum recommended VCM current is on the order of 2.5 A.

The three flexures were designed to be very stiff radially to ensure that the VCM coils remain in alignment with the magnets and highly compliant axially to keep the loaded resonance frequency of the suspended mirror frame as low as possible. The design analysis of the flexures assumed the etalon to be horizontal with the full mirror support weight on the flexure dimensions and material properties. The results are seen in Figure 5 which shows the static deflection and loaded resonance as functions of the flexure thickness. The graph may be used to determine a compromise between static deflection and tolerable resonance.

The fixed mirror frame is supported by two stainless steel rods against which the frame is pushed by a 1/4-20 plunger screw (11). The frame is retained radially by a key (19).

The mirrors are held in their respective frames by a radial spring shown in Figure 6. The 16 spring leaves are bent at a right angle to the ring to provide a purely radial compression of the mirror substrate, while an additional ring with truncated leaves that are left straight retains the mirror axially. An analysis of this retention technique showed that the maximum deformation of the substrate due to this compression is on the order of 1 microinch. This is well within the flatness criterion established for the substrates.

### The Reference Interferometer

The reference etalon is a Burleigh model RC-150 which is driven by a piezoelectric power supply that provides both static and dynamic alignment of its cavity mirror. A GaAs diode laser is used to align the interferometer using the piezoelectric ramp function generator to display the laser line on an oscilloscope.

After the reference etalon has been aligned the broad band GaAlAs light emitting diode (LED) is used to provide the required reference light. The LED light is collimated by a 9 mm focal length lens and refocussed on the other side of the etalon onto three contiguous fiberoptic cables which direct the radiation into the collimators at the periphery of IR interferometer as shown in Figure 4 (note 6). The fiberoptic cables from the reference etalon are connected to a bulkhead connector mounted on the dewar wall and connected internally to three fiberoptic cables specially designed to survive the cryogenic environment. A dual photodetector senses the light transmitted through the cavity mirrors which at their periphery have a reflective finesse on the order of 40. This is sufficient to provide the required calibration points for the Kaman sensors.

### The Central Processing Unit and Data Acquisition System

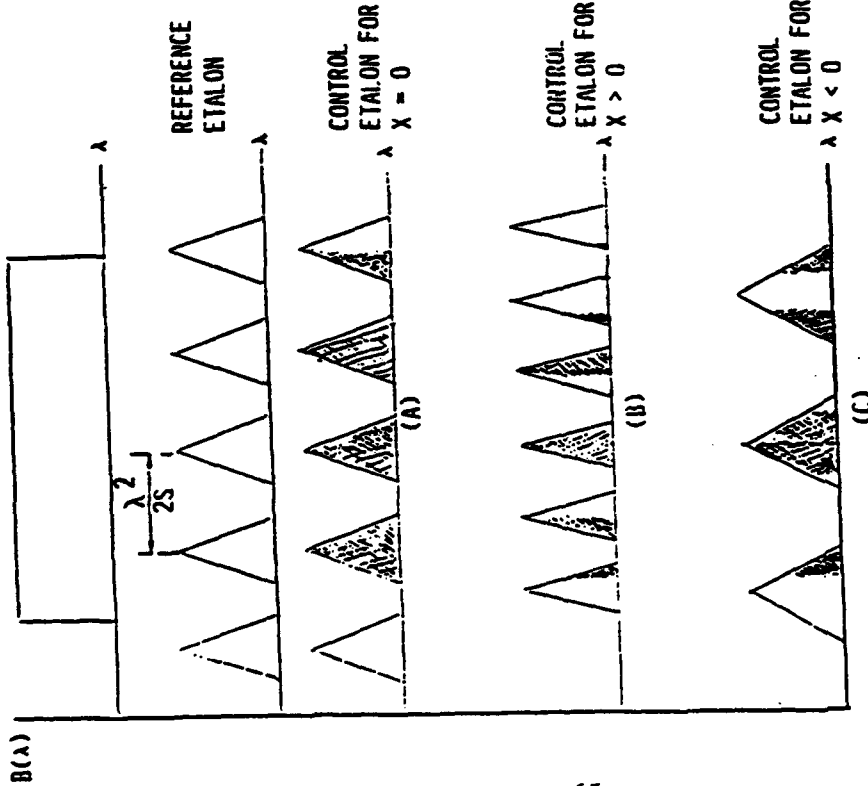
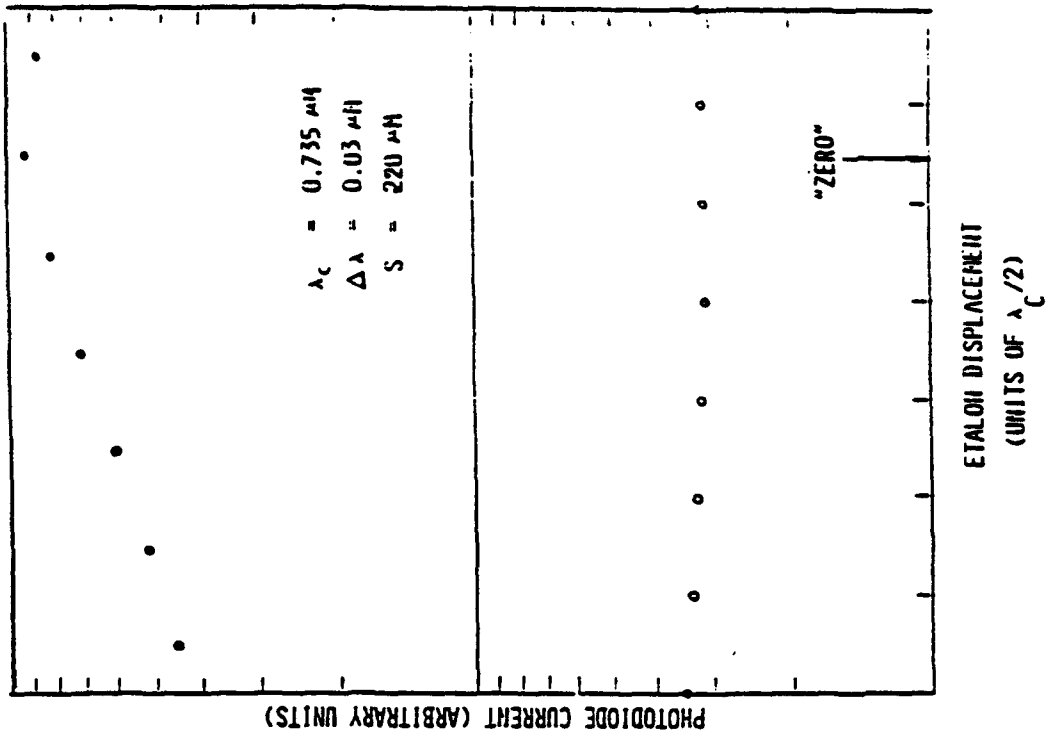
The F-P interferometer is controlled by an IBM PC/XT computer which is connected to the servo system via a Data translation model DT2827 data acquisition board and a Metrabyte P10-12 input-output board which relay the spectral scan commands and receive the Kaman sensor - and IR photodetector signals. The data flow block diagram in Figure 7 shows the instrument control concept.

The servo system analog commands are derived from the I/O board digital commands via three 18 bit D/A converters which have sufficient resolution to step the suspended mirror mount through the Kaman sensor calibration range and the free spectral range of the interferometer.

### Critical Parts Procurement

The critical parts of the interferometer consist of the cavity mirrors, the Kaman position sensors, and the BEI/Kimco VCM's. The latter two have been ordered from the catalogue of the respective manufacturer, while the cavity mirrors are custom made to specifications by Janos Technology. A conference with Janos technical personnel resulted in the following specifications:

1. Aperture (IR)	50 mm
2. Surface Flatness	1/20th wave (HeNe)
3. Reflectance (IR)	96% (4 $\mu$ m to 6 $\mu$ m)
4. Reflectance (periphery)	93% (0.7 $\mu$ m to 0.9 $\mu$ m)

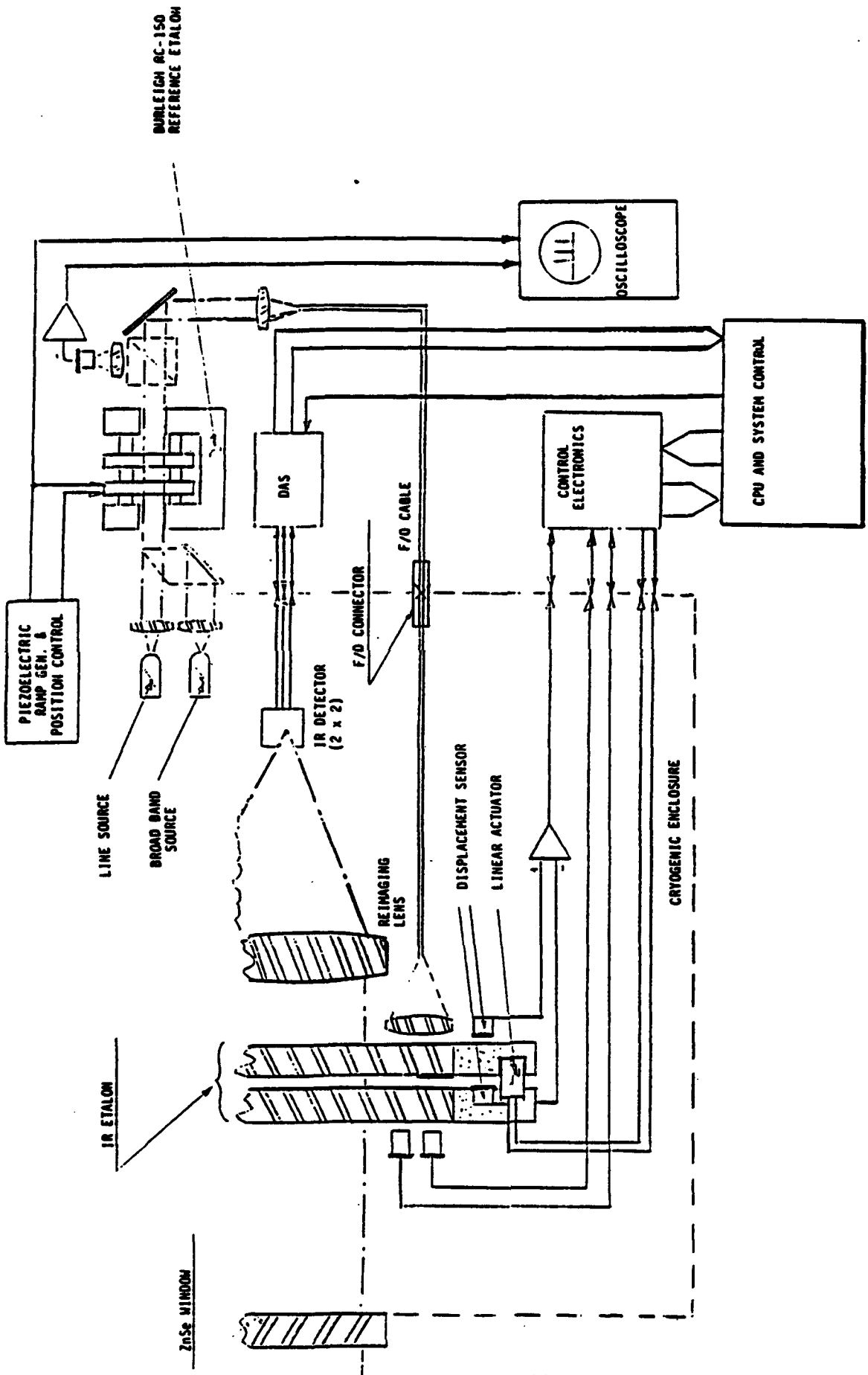


SCHEMATIC OF ETALON CONTROL CONCEPT

FIGURE 1.

$I(S, x)$  AS A FUNCTION OF  $x$

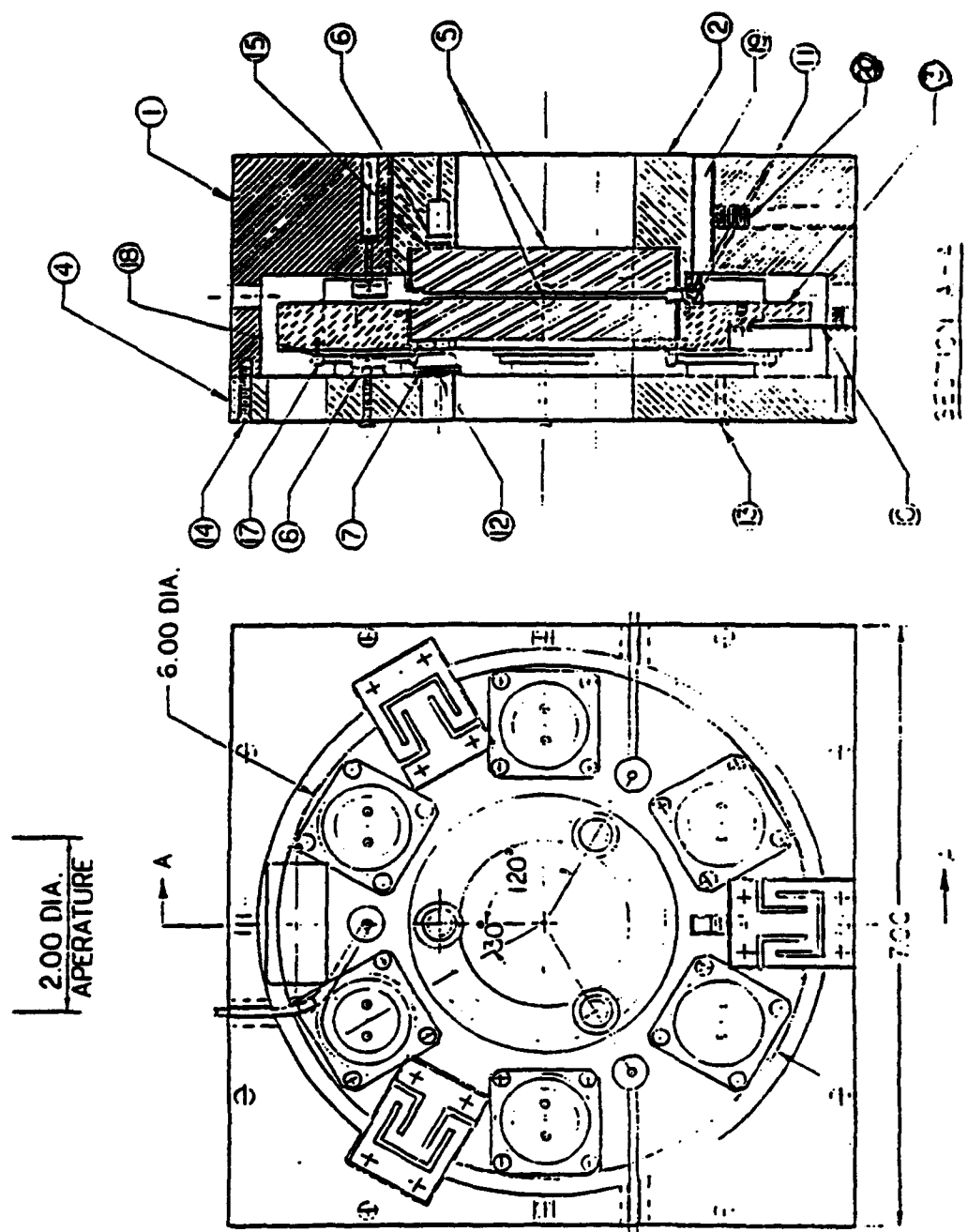
FIGURE 2.



FUNCTIONAL BLOCK DIAGRAM  
SSG FABRY-PEROT INTERFEROMETER

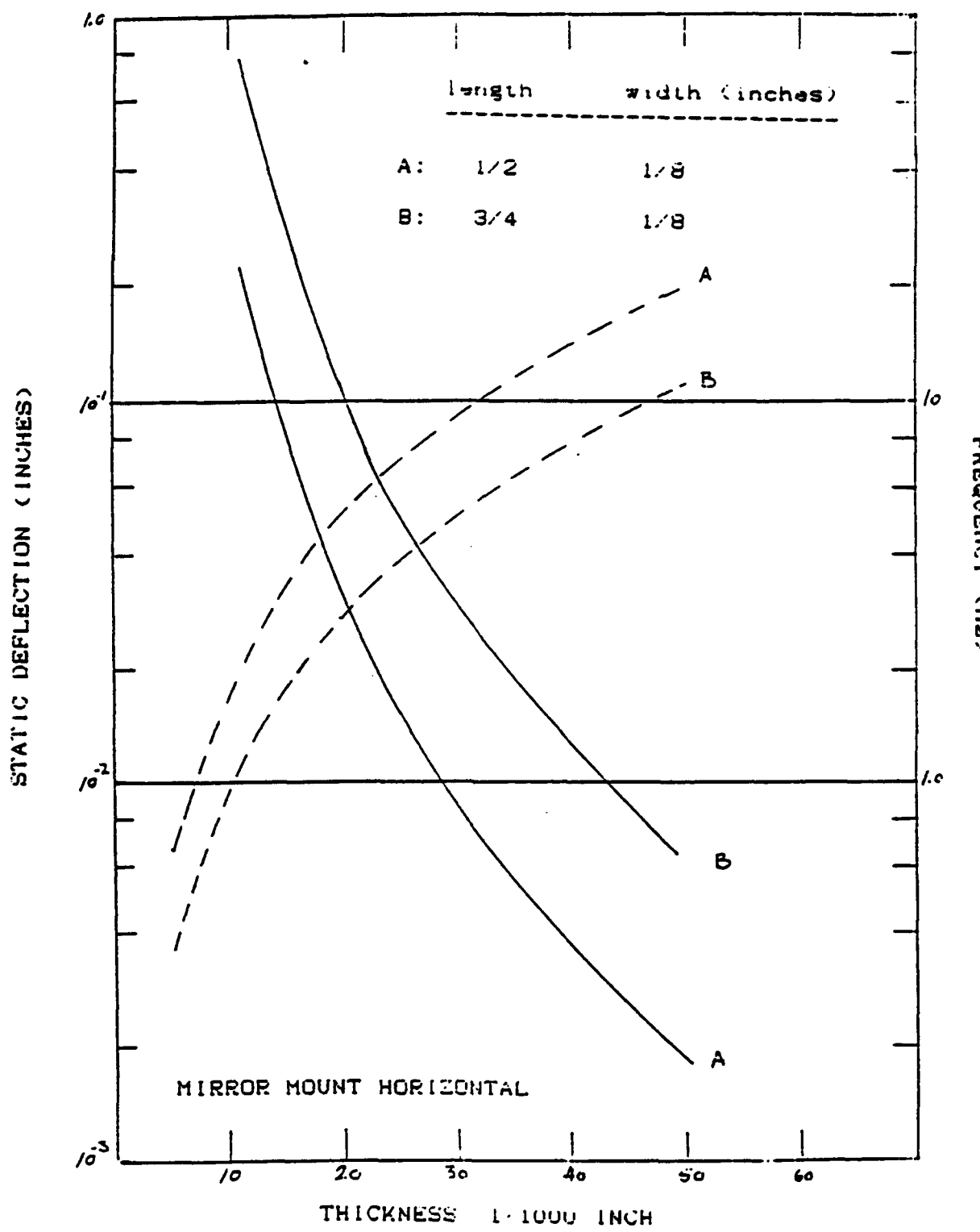
FIGURE 3.

1	Main Frame
2	Stationary Etalon Mount
3	Suspended Etalon Mount
4	Front Panel
5	Fabry-Perot Etalon Plate
6	12 mm Achromat
7	Dual Photodetector
8	Sensor (Kamex KD-5100-20N)
9	Linear Actuator (B&I LA10-12)
10	Suspension Flexure
11	Etalon Plate Retainer
12	Standoff, Insulating
13	Screw, Pan Head, #4-40X.620 lg.
14	Screw, Flat Head, #4-40X.75 lg.
15	Retainer, Lens
16	Retainer, Actuator
17	Screw, Pan Head, #2-56X.25 lg.
18	Nasher, #2 x .06 TH
19	Key, .250 x 1.25 lg.
20	Screw, Set, HP, 1/4-20X.38 lg.



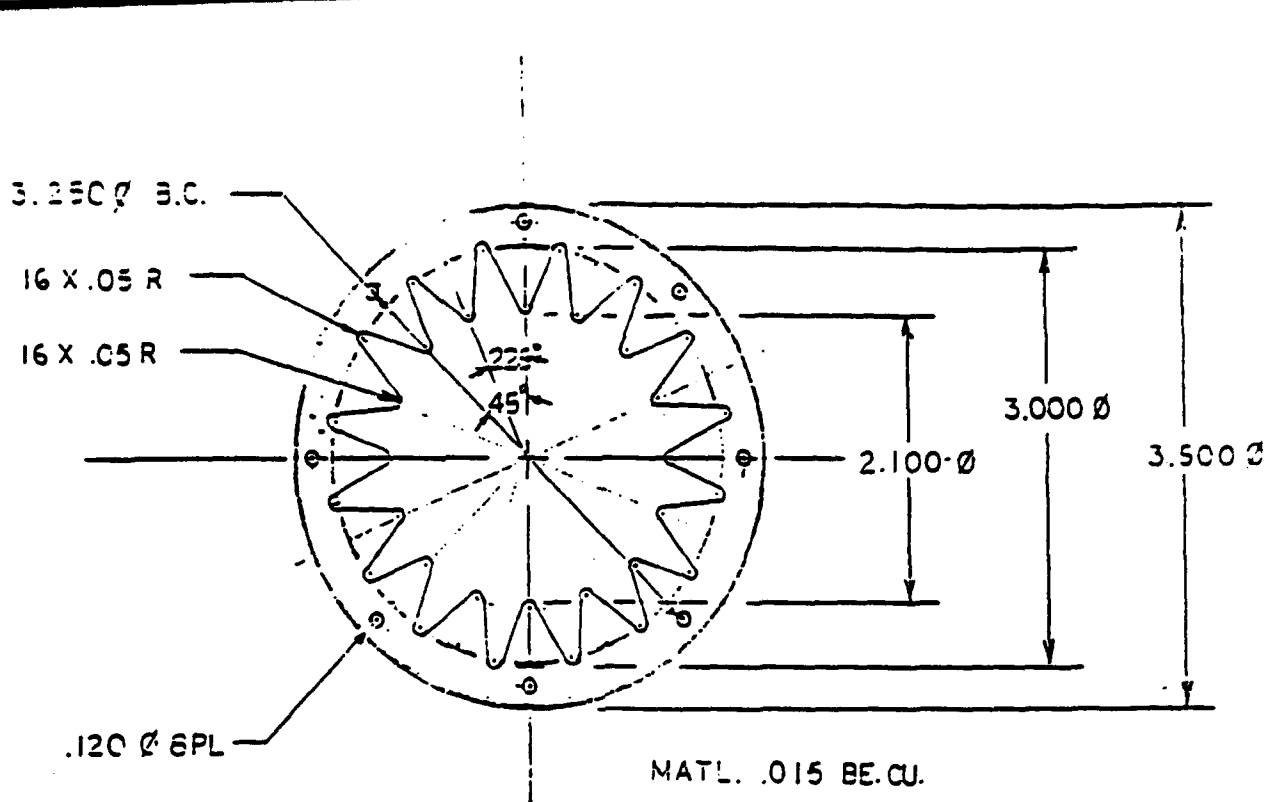
SSG FABRY-PEROT INTERFEROMETER  
MECHANICAL CONSTRUCTION

FIGURE 4.



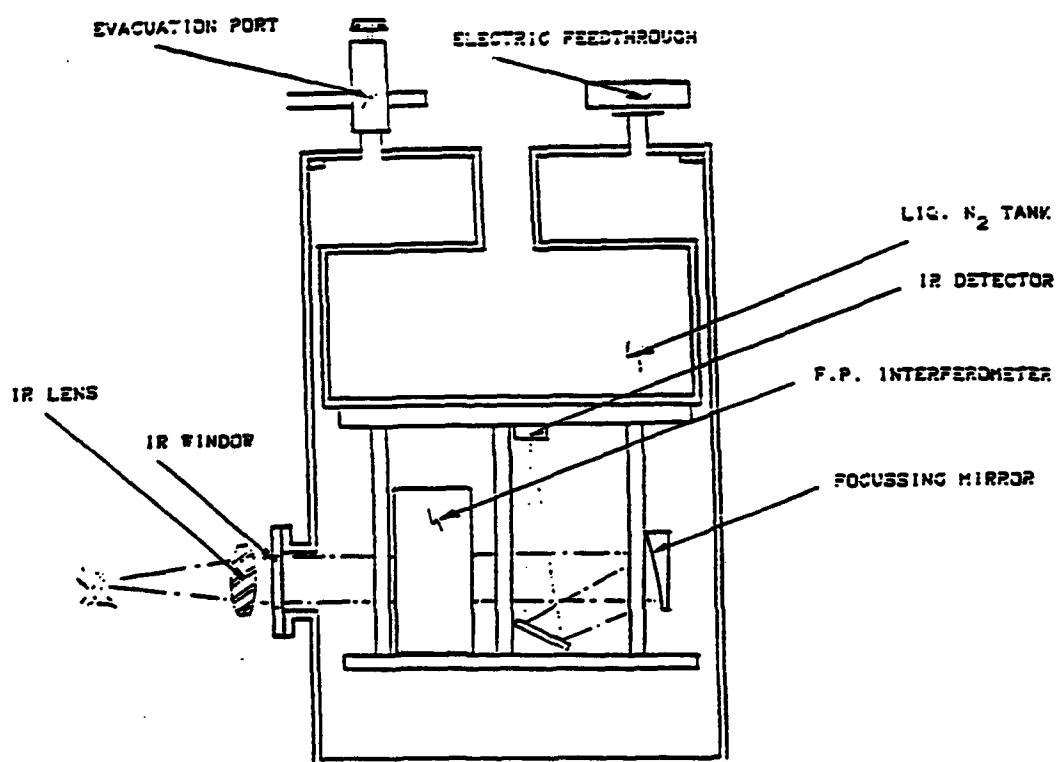
STATIC DEFLECTION & LOADED RESONANCE  
AS FUNCTION OF FLEXURE THICKNESS

FIGURE 5.



MIRROR RETENTION SPRING

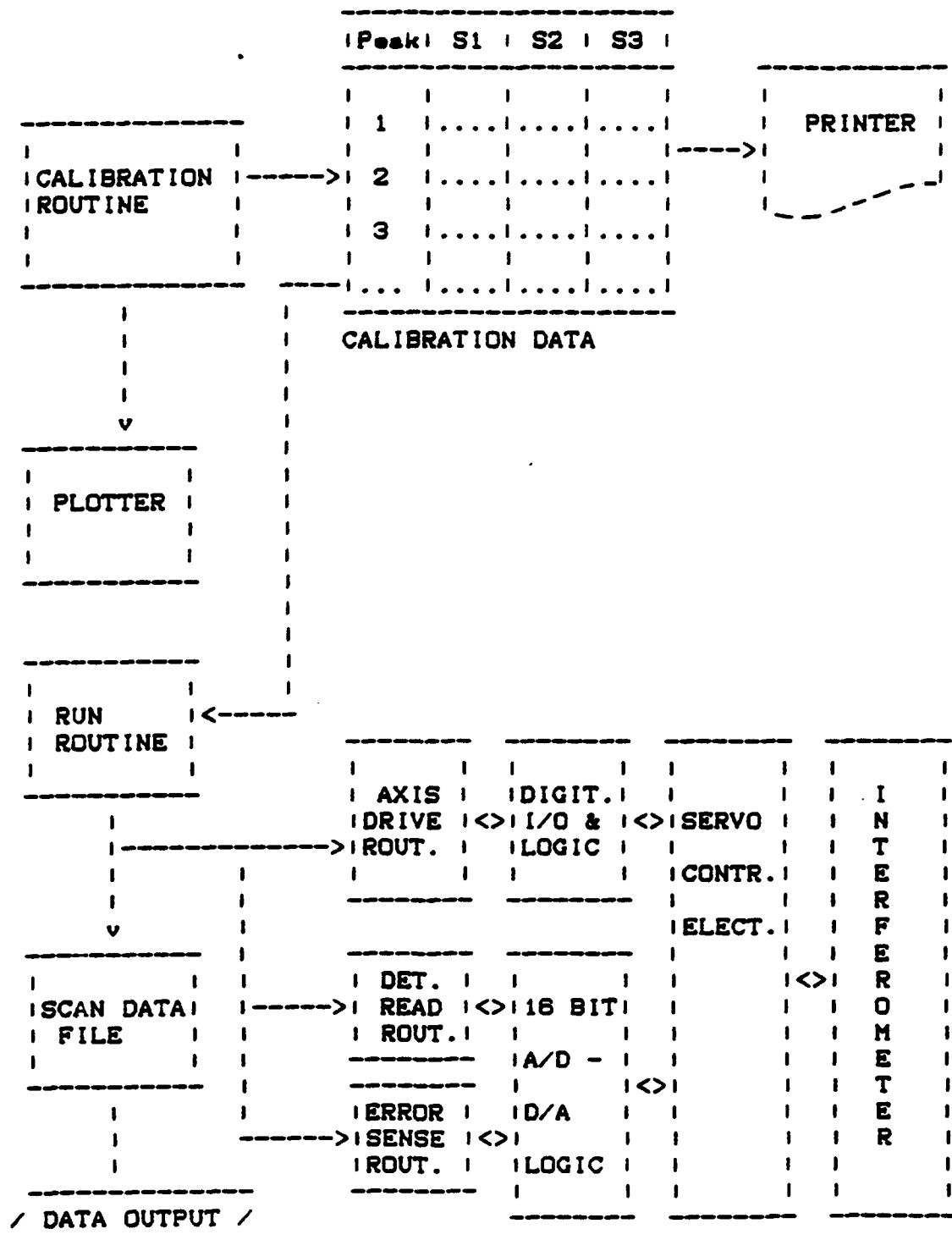
FIGURE 6.



DEWAR ASSEMBLY CROSS SECTIONAL

VIEW

FIGURE 8.



INTERFEROMETER SYSTEM DATA FLOW  
FIGURE 7.

5. Wedge	> 1 min.
6. Substrate mat'l	Cleartran ZnS
7. Scratch/dig	40/20
8. A/R coating	$T \geq 95\%$ in IR

### The Cryogenic Dewar

The liquid nitrogen dewar used to demonstrate the instruments performance is a side looking stainless steel canister manufactured by Janis Research Co. It is shown in cross-section in Figure 8 which also illustrates the anticipated installation of the interferometer and the detector. The dewar is not purchased for this contract and will remain with SSG, Inc.

### Bibliography

1. H. A. Smith, J. Fischer, W. B. Waltman, et. al, Opt. Eng. 24, 275-84, 1985.
2. J. V. Ramsey, Appl. Opt. 5, 1297, 1966.
3. P. Jacquinot, Repts, Prog. Phys. 23, 267-312, 1960.
4. G. Hernandez, Fabry-Perot Interferometers, Cambridge Studies in Modern Optics 3, Cambridge Univ. Press 1986.

## PHASE 2 - HARDWARE PHASE

### 1.0 INTRODUCTION

The SSG cryogenic etalon system was being developed for the Air Force Geophysical Laboratories (AFGL) scientific rocket and balloon experiments. The instrument provides stabilization of the etalon mirror cavity to a parallelism equal to or better than 0.2 arcseconds over a servo system bandwidth of 100 Hz. The mirror cavity spacing is controlled by six voice coil motors (VCM's) which are driven by three servo systems which each use a Kaman 5100 series differential eddy current sensor to measure the relative separation of the two etalon mirrors. The Kaman sensors have a noise equivalent displacement of  $1 \times 10^{-7}$  mm/(Hz)<sup>1/2</sup> and are therefore capable of resolving differential displacements on the order of 10 nanometers at a signal to noise level of 10:1. The moveable mirror is supported on an aluminum frame which in turn is suspended from the main frame by three flexures that have high axial compliance while retaining a sufficient radial stiffness to maintain the alignment of the VCM coils in their respective armatures. Figure 1-1 shows the prototype hardware.

The mechanical design of the etalon is seen to have a measured open loop response shown in Figure 1-2. The loaded resonance peaks of the linear flexures are located at approximately 15 and 18 Hz. These frequencies represent a good compromise between allowable (uncontrolled) static deflection and the requirement of having the lowest feasible natural resonance. The open loop response was found to be free of parasitic mechanical resonances except for a rather prominent peak at 1.2 KHz. This vibration was determined to be the fundamental resonance of the mirror support plate. This resonance, however, was sufficiently far from the servo system's corner frequency to be of no concern. Figure 1-2a shows the closed loop frequency response of the FPIRS.

The principal features of the servo system are shown in the block diagram in Figure 1-3. The photodiode cells shown in the diagram are used to calibrate the Kaman sensors which are in the control loop. The system is controlled from the keyboard of an IBM AT computer. The resolution of the D/A converters controlling the actuators is required to be 18 bits. The 18 bits are necessary to step the etalon mirror spacing over its free spectral range in increments of its  $0.5 \text{ cm}^{-1}$  spectral resolution.

### 2.0 Final Program Status.

As of the date of termination of this program the following tasks were completed:

SSU FABRY-PEROT INFRARED SPECTROMETER

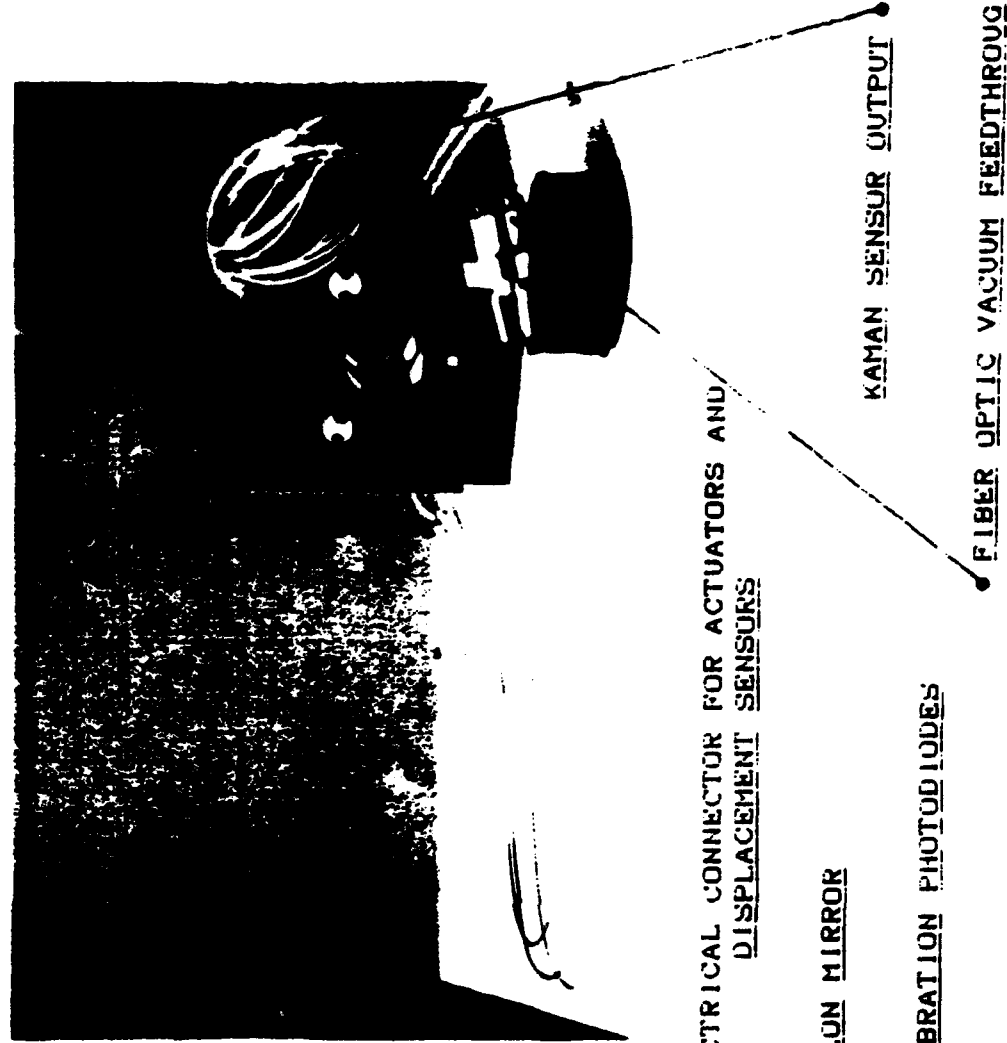


FIGURE 1-1.

FIGURE 1-2.

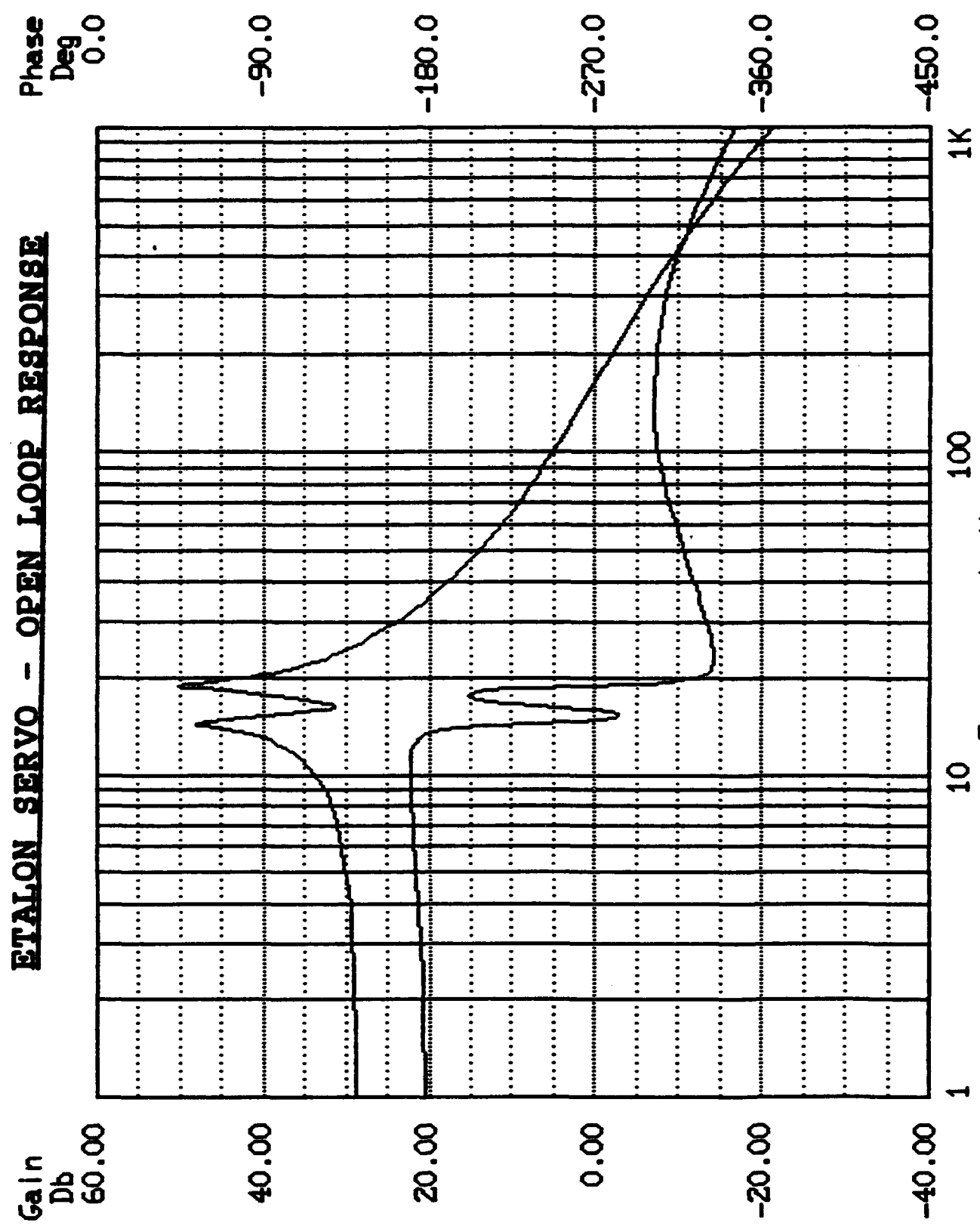
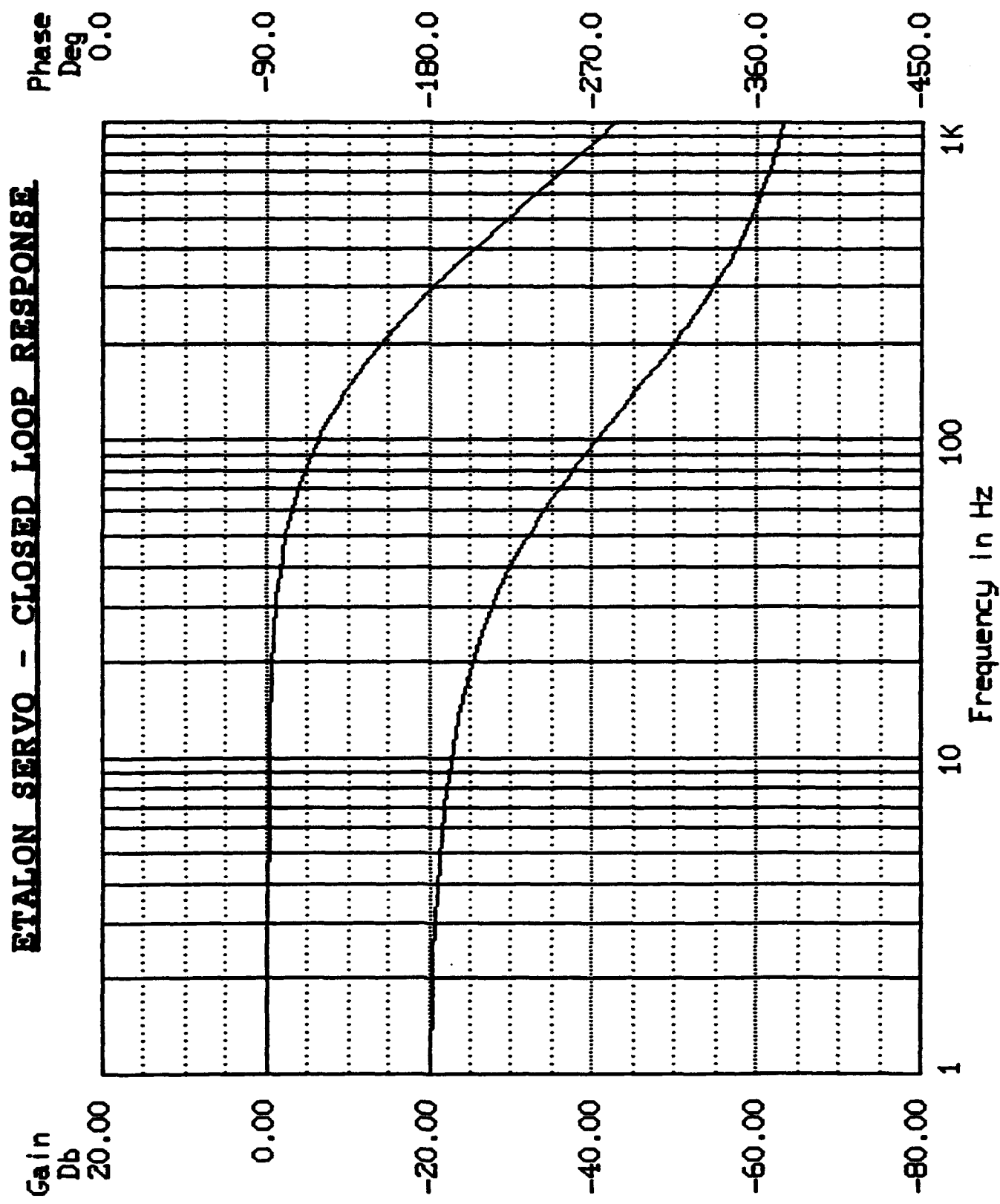
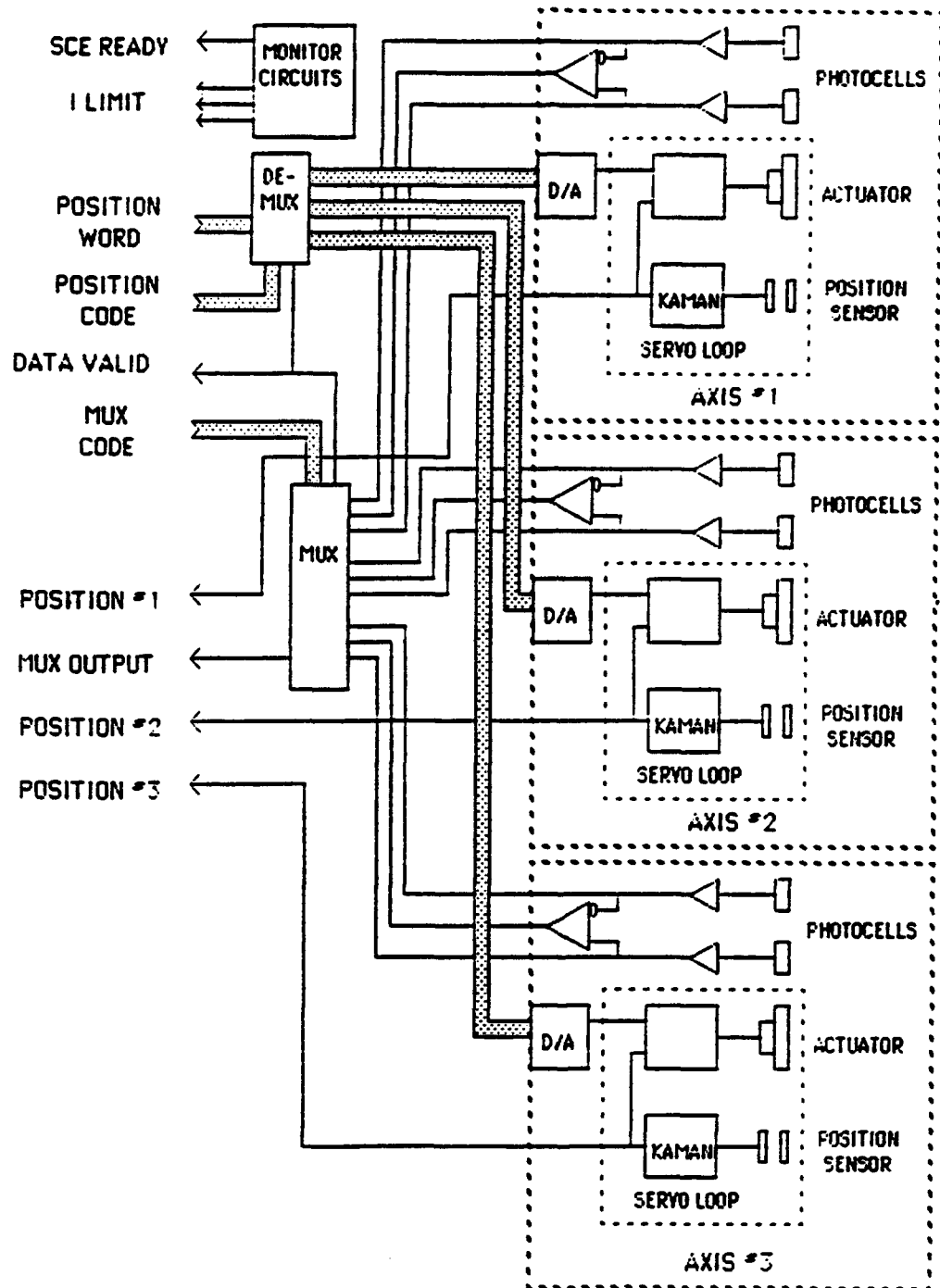


FIGURE 1-2a



**BLOCK DIAGRAM - SCE ELECTRONICS**



**SSG CRYOGENIC ETALON CONTROL  
ELECTRONICS - BLOCK DIAGRAM**

**FIGURE 1-3.**

1. Procurement of all required components inclusive of the etalon mirrors the finesse of which is shown in Figure 1-4, the actuators, Kaman sensors, fiberoptic cables and sensors, the Burley reference etalon, and all machined and photoetched parts comprising the prototype unit.
2. Experimental verification of the transmittance of the fiberoptic cable system to ascertain that its total attenuation did not exceed 8 dB (measured attenuation: 5.5 dB).
3. Experimental verification of closed loop response of the mirror servo system. This was accomplished with the moving mirror configured in a Michelson interferometer. This activity led to the conclusion that the servo required a velocity loop to prevent a slow oscillation of the mirror system about its nominal position as sensed by the Kaman sensors.
4. Formulated the digital interface to control the interferometer from the PC and formatted the correction look-up tables for the three sensors (and actuators).
5. Designed and procured the absorption cell, spectral order sorting filters, and light source to provide the prototype etalon with a known spectral source against which the unit could be calibrated.
6. Designed the cryogenic fixture to test the unit at 77° K in a cryostat with a ZnS (Cleartran) window.
7. Assembled the prototype etalon system using the Fabry-Perot mirrors fabricated by Janos Technology.

Ongoing activities at the time of termination of this program included the integration of the velocity loop into the servo system, a final review of the fixtures for the cryostat prior to their fabrication, the integration of the spectral source facility, final system check-out of the prototype unit, and its integration with the servo system.

FIGURE 1-4.

